

## Impact of Upper Ocean–Topographical Coupling and Isopycnal Outcropping in Japan/East Sea Models with $1/8^\circ$ to $1/64^\circ$ Resolution\*

PATRICK J. HOGAN AND HARLEY E. HURLBURT

*Naval Research Laboratory, Stennis Space Center, Mississippi*

(Manuscript received 3 November 1998, in final form 23 November 1999)

### ABSTRACT

A regional primitive equation ocean model is used to investigate the impact of grid resolution, baroclinic instability, bottom topography, and isopycnal outcropping on the dynamics of the wind and throughflow-forced surface circulation in the Japan/East Sea. The results demonstrate that at least  $1/32^\circ$  (3.5 km) horizontal grid resolution is necessary to generate sufficient baroclinic instability to produce eddy-driven cyclonic deep mean flows. These abyssal currents follow the  $f/h$  contours of the bottom topography and allow the bottom topography to strongly influence mean pathways of the upper-ocean currents in the Japan/East Sea. This upper ocean–topographical coupling via baroclinic instability (actually a mixed baroclinic–barotropic instability) requires that mesoscale variability be very well resolved to obtain sufficient coupling. For example,  $1/32^\circ$  resolution is required to obtain a realistic separation latitude of the East Korean Warm Current (EKWC) from the Korean coast when Hellerman–Rosenstein monthly climatological wind stress forcing is used. Separation of the EKWC is more realistic at  $1/8^\circ$  resolution when the model is forced with climatological winds formed from the ECMWF 10-m reanalysis due to strong positive wind stress curl north of the separation latitude, but at  $1/8^\circ$  the level of baroclinic instability is insufficient to initiate upper ocean–topographical coupling. Hence, this major topographical effect is largely missed at coarser resolution and leads to erroneous conclusions about the role of bottom topography and unexplained errors in the pathways of current systems. Results from a  $1/64^\circ$  simulation are similar to those at  $1/32^\circ$ , particularly where the EKWC separates from the Korean coast, suggesting statistical simulation convergence for mesoscale variability has been nearly achieved at  $1/32^\circ$  resolution. Isopycnal outcropping and associated vertical mixing provide an alternate mechanism to topographical control in developing and maintaining a boundary current along the west coast of Japan, but are less important than baroclinic instability in driving deep mean flows.

### 1. Introduction

Located between Japan, Korea, and Russia, the Japan/East Sea (hereafter referred to as the JES) is a part of the chain of adjacent marginal seas in the northwest Pacific. With a maximum depth of about 3700 m, the JES has been characterized as a microcosm of the global ocean (Ichiye 1984). Indeed, large-scale circulation features similar to those found in the global ocean include cyclonic and anticyclonic gyre systems, a western boundary current that separates from the coast, and a deep homogeneous water mass. Other interesting phenomena include wind and thermal-driven circulation, deep convection, and a

ubiquitous mesoscale eddy field. Because the JES contains processes similar to those occurring in large-scale ocean basins, but is smaller and may adjust more rapidly, and hence be easier to study, the JES offers ocean scientists a unique natural laboratory for investigating oceanic processes. For the same reasons, the JES is an ideal basin for studying dynamics via numerical simulations. The region is characterized by complex circulation patterns and mesoscale variability, yet is small enough for multiple simulations to be economically feasible, including some with very high horizontal grid resolution. This feasibility is further enhanced by using the Naval Research Laboratory's Layered Ocean Model (NLOM), a modular design that provides an effective means to dissect ocean dynamics (Hurlburt et al. 1996) and one that is extremely efficient and portable to several different computer architectures (Wallcraft and Moore 1997).

Inflow through Tsushima Strait and outflow through the Tsugaru and Soya Straits (Fig. 1) couples the JES to the Pacific Ocean. These straits have shallow sill depths; the deepest sill depth (about 200 m) is in the

\* Naval Research Laboratory Contribution Number NRL/JA 7323-98-0063.

Corresponding author address: Dr. Patrick J. Hogan, Naval Research Laboratory, Stennis Space Center, MS 39529-5004.  
E-mail: hogan@barracuda.nrlssc.navy.mil

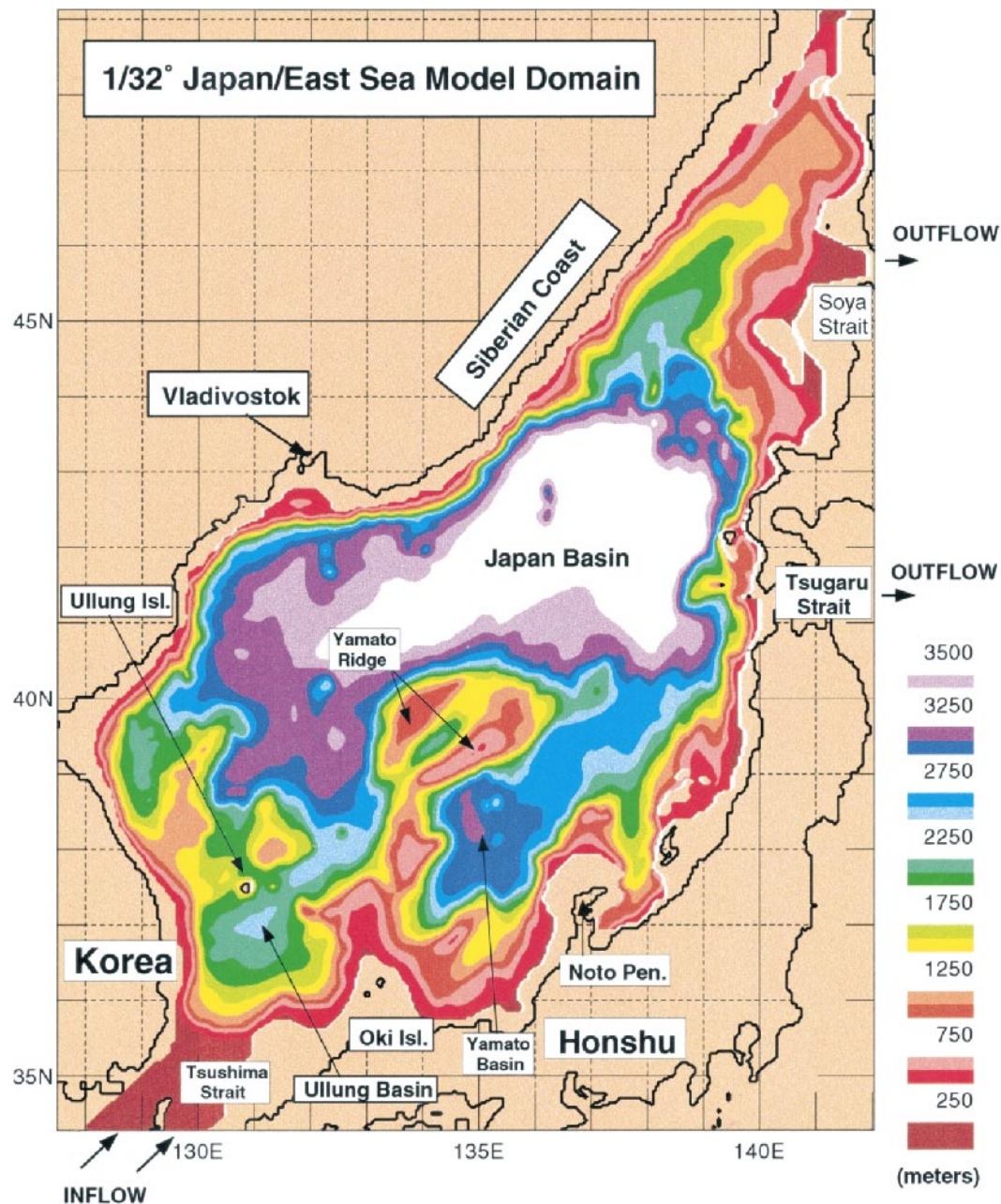


FIG. 1. THE  $\frac{1}{32}^\circ$  bottom topography for the Japan/East Sea. Locations of the inflow and outflow ports are marked as black arrows. Geographical locations used in text are marked. Contour interval is 250 m.

western channel of Tsushima Strait. However, flow through these straits has a profound impact on the circulation features within the JES. In particular, a fundamental circulation feature in the JES is the Tsushima Warm Current (TWC), which transports warm salty water into the basin through Tsushima Strait. The historical interpretation of Suda and Hidaka (1932) and Uda (1934) that the TWC splits into three distinct branches after entering the basin is still widely accepted, but others (Moriyasu 1972) have regarded the TWC as a single

meandering current that episodically sheds eddies. The highly variable spatial and temporal characteristics of the TWC make it difficult to support one theory over the other. Indeed, hydrographic surveys (Kawabe 1982; Kim and Chung 1984), analyses of satellite infrared data (Kim and Legeckis 1986; Cho and Kim 1996), and analysis of satellite-tracked drifters (Beardsley et al. 1992) demonstrate the complex and chaotic behavior of this current system.

In contemporary literature, the three branches of the

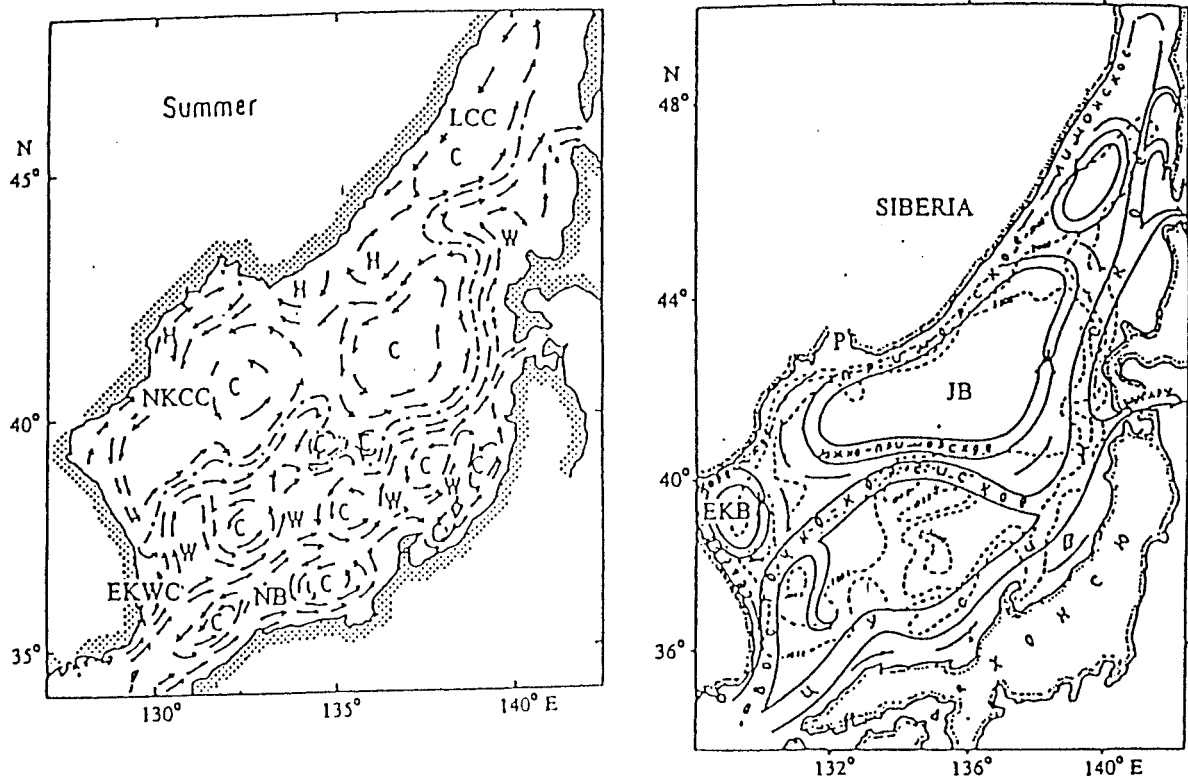


FIG. 2. Observationally based schematic patterns of surface circulation in the Japan/East Sea (a) in summer by Naganuma (1977) and (b) annual mean by Yarichin (1980). The following currents are labeled: East Korea Warm Current (EKWC), Nearshore Branch (NB), Liman Cold Current (LCC), and North Korea Cold Current (NKCC). Warm (cold) rings are denoted by a "W" ("C"). From Preller and Hogan (1998).

TWC (from east to west) are named the Nearshore Branch (NB), the Offshore (or Middle) Branch, and the East Korea Warm Current (EKWC), respectively. In the three-branch view, the NB flows eastward along the coast of Honshu and exits into the Pacific Ocean through Tsugaru Strait (Fig. 2). The Offshore Branch, which is more variable in space and time, is situated to the west-northwest of the Nearshore Branch and flows along Honshu farther offshore. The EKWC flows northward along the Korean continental slope to about  $37^{\circ}$ – $38^{\circ}$ N, where it meets the southward flowing North Korean Cold Current (NKCC). At the confluence, the currents separate from the coast and flow east-northeast toward Tsugaru Strait along the polar front. Much of that flow exits through Tsugaru Strait, while the remainder continues northward along the coast of Hokkaido as the Tsugaru Warm Current. Some of this flow exits into the Sea of Okhotsk through Soya Strait, while the remainder eventually returns southward along the Siberian coast as the Liman (or Primoriye) Cold Current (LCC) and the NKCC (south of Vladivostok), forming a cyclonic gyre in the northern part of the basin (Fig. 2).

A primary objective of this study is to identify the critical dynamical processes responsible for the observed and modeled circulation patterns in the JES. For

instance, what mechanism determines the separation latitude of the EKWC from the coast of Korea? What causes the formation and persistence of the NB of the TWC? What role does the bottom topography play in influencing the surface circulation? Of course the ability to address questions such as these depends on the realism of the numerical model being used to investigate the dynamics. The realism of any given simulation is dependent on many criteria, including choice of model physics, numerical implementation of the equations of motion, the choice of forcing functions and parameter space, and model grid resolution. For the simulations used in this study, the numerical implementation of the equations of motion is identical for all simulations (see Hurlburt and Thompson 1980; Wallcraft 1991; Hurlburt et al. 1996; Moore and Wallcraft 1998). The model physics are varied only to the extent that they are used to explore the parameter space for the simulations. The primary forcing functions are inflow and outflow through the straits and monthly climatological wind stress. Nearly all of the simulations are forced with seasonally varying inflow and outflow through the straits and the Hellerman and Rosenstein (1983, hereafter HR) monthly wind stress climatology, although that wind climatology may not give the best results in the JES.

Indeed, a simulation forced with a different wind set is offered to accentuate this point. However, because we are interested in the *dynamics* of the circulation, a less than optimal wind set can actually facilitate this task because systematic changes between different solutions can be easier to identify.

The overall strategy employed in this study is to exploit the modularity of the NLOM to investigate the circulation dynamics in the JES. In this context we examine the solutions from an ensemble of simulations with increasing (dynamical) complexity by including or excluding certain features and dynamical processes. The simplest end-member in this ensemble is a linear 1.5-layer reduced-gravity design, while the most complex is a fully nonlinear 4-layer design with realistic bottom topography. Information on the model design is discussed in section 2 and specific details of the model implementation for the JES are presented in section 3. In section 4 the lowest order dynamics of the JES are investigated with a series of linear  $\frac{1}{8}^\circ$ , 1.5-layer reduced-gravity simulations. In section 5 we examine the sensitivity to external forcing, as well as the impact of higher order dynamics, such as nonlinearity and isopycnal outcropping. The impacts of horizontal grid resolution, mesoscale flow instabilities, and realistic bottom topography are discussed in section 6. In these simulations, horizontal grid resolution varies from  $\frac{1}{8}^\circ$  (14 km) to  $\frac{1}{64}^\circ$  (1.7 km), which allows the role of upper ocean–topographical coupling to be examined in detail.

Finally, the summary and conclusions are presented in section 7.

## 2. The NRL Layered Ocean Model (NLOM)

The NLOM is a semi-implicit primitive equation ocean model with vertically integrated model equations for each layer. In the NLOM, the layered model equations are cast in transport form and (in the version used here) the interfaces between the layers are isopycnal surfaces. The model retains the free surface and can include realistic bottom topography as long as it is confined to the lowest layer. The fundamental model design is described in detail in Hurlburt and Thompson (1980), although Wallcraft (1991) has significantly enhanced the current version. The mathematical and numerical formulation of the equations in spherical coordinates are discussed in Moore and Wallcraft (1998), with particular attention given to the proper formulation of the isopycnal diffusion. The simulations for this study use a portable, scalable version of the NLOM (Wallcraft and Moore 1997), which runs efficiently and interchangeably on a wide variety of computer architectures using a tiled data parallel programming paradigm.

The equations for the  $n$ -layer finite depth, hydrodynamic model are given below for layers  $k = 1, \dots, n$  with  $k = 1$  for the top layer. In places where  $k$  is used to index model interfaces,  $k = 0$  is the surface and  $k = n$  is the bottom:

$$\begin{aligned} & \left[ \frac{\partial U_k}{\partial t} + \frac{1}{a \cos \theta} \left[ \frac{\partial(U_k u_k)}{\partial \phi} + \frac{\partial(V_k u_k \cos \theta)}{\partial \theta} - V_k(u_k \sin \theta + a\Omega \sin 2\theta) \right] \right. \\ & = + \max(0, -\omega_{k-1})u_{k-1} + \max(0, \omega_k)u_{k+1} - (\max(0, -\omega_k) + \max(0, \omega_{k-1}))u_k \\ & \quad + \max(0, -C_M \omega_{k-1})(u_{k-1} - u_k) + \max(0, C_M \omega_k)(u_{k+1} - u_k) - \frac{h_k}{a \cos \theta} \sum_{j=1}^n G_{kj} \frac{\partial(h_j - H_j)}{\partial \phi} \\ & \quad \left. + (\tau_{\phi_{k-1}} - \tau_{\phi_k})/\rho_o + \frac{A}{a^2 \cos^2 \theta} \left[ \frac{\partial(h_k e_{\phi \phi_k} \cos \theta)}{\partial \phi} + \frac{\partial(h_k e_{\phi \theta_k} \cos^2 \theta)}{\partial \theta} \right] \right] \quad (1) \end{aligned}$$

$$\begin{aligned} & \left[ \frac{\partial V_k}{\partial t} + \frac{1}{a \cos \theta} \left[ \frac{\partial(U_k v_k)}{\partial \phi} + \frac{\partial(V_k v_k \cos \theta)}{\partial \theta} + U_k(u_k \sin \theta + a\Omega \sin 2\theta) \right] \right. \\ & = + \max(0, -\omega_{k-1})v_{k-1} + \max(0, \omega_k)v_{k+1} - (\max(0, -\omega_k) + \max(0, \omega_{k-1}))v_k \\ & \quad + \max(0, -C_M \omega_{k-1})(v_{k-1} - v_k) + \max(0, C_M \omega_k)(v_{k+1} - v_k) - \frac{h_k}{a} \sum_{j=1}^n G_{kj} \frac{\partial(h_j - H_j)}{\partial \theta} \\ & \quad \left. + (\tau_{\theta_{k-1}} - \tau_{\theta_k})/\rho_o + \frac{A}{a^2 \cos^2 \theta} \left[ \frac{\partial(h_k e_{\phi \theta_k} \cos \theta)}{\partial \phi} + \frac{\partial(h_k e_{\theta \theta_k} \cos^2 \theta)}{\partial \theta} \right] \right] \quad (2) \end{aligned}$$

$$\frac{\partial h_k}{\partial t} + \nabla \cdot \mathbf{V}_k = \omega_k - \omega_{k-1} - \hat{K}_4 \nabla^2 [\nabla^2 (h_k - H_k)], \quad (3)$$

where

$$\nabla \cdot \mathbf{F} = \frac{1}{a \cos \theta} \frac{\partial F_\phi}{\partial \phi} + \frac{1}{a \cos \theta} \frac{\partial (F_\theta \cos \theta)}{\partial \theta}$$

$$\nabla^2 \Phi = \frac{1}{a^2 \cos^2 \theta} \frac{\partial^2 \Phi}{\partial \phi^2} + \frac{1}{a^2 \cos \theta} \frac{\partial}{\partial \theta} \left( \frac{\partial \Phi}{\partial \theta} \cos \theta \right)$$

$h_k$  =  $k$ th layer thickness

$\mathbf{v}_k$  =  $k$ th layer velocity =  $\tilde{\mathbf{e}}_\phi u_k + \tilde{\mathbf{e}}_\theta v_k$

$\mathbf{V}_k = h_k \mathbf{v}_k = \tilde{\mathbf{e}}_\phi U_k + \tilde{\mathbf{e}}_\theta V_k$

$\tilde{\mathbf{e}}_k$  = angular deformation tensor

$$e_{\phi\phi k} = \frac{\partial}{\partial \phi} \left( \frac{u_k}{\cos \theta} \right) - \cos \theta \frac{\partial}{\partial \theta} \left( \frac{v_k}{\cos \theta} \right) = -e_{\theta\theta k}$$

$$e_{\phi\theta k} = \frac{\partial}{\partial \phi} \left( \frac{v_k}{\cos \theta} \right) + \cos \theta \frac{\partial}{\partial \theta} \left( \frac{u_k}{\cos \theta} \right) = e_{\theta\phi k}$$

$H_k$  =  $k$ th layer thickness at rest

$$H_n = D(\phi, \theta) - \sum_{j=1}^{n-1} H_j$$

$D(\phi, \theta)$  = total depth of the ocean at rest

$\rho_0$  = constant reference density

$\rho_k$  =  $k$ th layer density, constant in space and time

$$G_{kj} = \begin{cases} g & j \geq k \\ g - g(\rho_k - \rho_j)/\rho_0 & j < k \end{cases}$$

$\boldsymbol{\tau}_w$  = wind stress

$C_k$  = coefficient of interfacial friction

$C_b$  = coefficient of bottom friction

$$\boldsymbol{\tau}_k = \begin{cases} \boldsymbol{\tau}_w, & \text{for } k = 0 \\ C_k \rho_0 |\mathbf{v}_k - \mathbf{v}_{k+1}| (\mathbf{v}_k - \mathbf{v}_{k+1}), & \text{for } k = 1, \dots, n-1 \\ C_b \rho_0 |\mathbf{v}_n| \mathbf{v}_n, & \text{for } k = n \end{cases}$$

$$\omega_k = \begin{cases} 0 & \text{for } k = 0, n \\ \omega_k^+ - \omega_k^- - W_k \hat{\omega}_k & \text{for } k = 1, \dots, n-1 \end{cases}$$

$$\omega_k^+ = \tilde{\omega}_k [\max(0, h_k^+ - h_k)/h_k^+]^2$$

$$\omega_k^- = \tilde{\omega}_k [\max(0, h_k - h_k^-)/h_k^+]^2$$

$$\hat{\omega}_k = (\omega_k^+ - \omega_k^-) / W_k$$

$\tilde{\omega}_k$  =  $k$ th interface reference diapycnal mixing velocity

$h_k^+$  =  $k$ th layer thickness at which entrainment starts

$h_k^-$  =  $k$ th layer thickness at which detrainment starts

$W_k(\phi, \theta)$  =  $k$ th interface weighting factor for global diapycnal mixing designed to conserve mass within a layer in compensation for explicit diapycnal mixing due to  $h_k < h_k^+$  (i.e.,  $\omega_k^+ - \omega_k^-$ ), and net transport through the lateral boundaries of layer  $k$

$C_M$  = coefficient of additional interfacial friction associated with entrainment

$A$  = coefficient of isopycnal eddy viscosity

$\overline{X(\phi, \theta)}$  = region wide area average of  $X$

$\hat{K}_4$  = coefficient of biharmonic horizontal layer thickness diffusivity

$a$  = radius of the Earth (6371 km)

$g$  = acceleration due to gravity (9.8 m s<sup>-2</sup>)

$t$  = time

$\Omega$  = angular rotation rate of the earth (7.292 205 × 10<sup>-5</sup> s<sup>-1</sup>)

$\theta$  = latitude

$\phi$  = longitude.

A hydrodynamic reduced-gravity model with  $n$  active layers has the lowest layer infinitely deep and at rest, that is,  $\mathbf{v}_{n+1} = 0$ ,  $h_{n+1} = \infty$ , and  $\nabla h_{n+1} = 0$ . The model equations for the active layers are identical to those for  $n$ -layer hydrodynamic finite depth model, except that

$$H_n = \text{const}$$

$$G_{kl} = g(\rho_{n+1} - \rho_k)/\rho_0, l \leq k$$

$$G_{kl} = g(\rho_{n+1} - \rho_l)/\rho_0, l > k$$

$$\boldsymbol{\tau}_k = \boldsymbol{\tau}_w, k = 0$$

$$\boldsymbol{\tau}_k = C_k \rho_0 |\mathbf{v}_k - \mathbf{v}_{k+1}| (\mathbf{v}_k - \mathbf{v}_{k+1}), k = 1, \dots, n$$

$$\omega_k = 0, k = 0$$

$$\omega_k = \max(0, \omega_k^+) - \max(0, \omega_k^-) - h_k \hat{\omega}_k, k = 1, \dots, n$$

The model equations were integrated on a C-grid (Mesinger and Arakawa 1976) using second-order, centered finite differences in space. The integrations in time used an explicit numerical scheme for the reduced-gravity simulations and a semi-implicit scheme for the finite depth simulations. For the finite depth simulations, the external and internal gravity waves are treated semi-implicitly in a manner similar to that described by Kwizak and Robert (1971). This treatment allows a longer time step than required for primitive equation models that use an explicit free surface or a rigid lid. Overall, the model is up to 100 times more efficient (in terms of central processing time per model year for a given domain and horizontal resolution) than existing fixed-level primitive equation ocean models (Wallcraft 1991).

An important attribute of the NLOM is the ability to allow isopycnal outcropping via ventilation of model interfaces. This process, called *hydromixing* (Wallcraft 1991), prevents nonpositive layer thickness, allows overturning cells in the vertical, and permits the existence of relatively thin layers. In practice, when a layer becomes thinner than a specified thickness  $h_k^+$ , fluid is entrained into it from the layer below, although there is no net transfer of fluid between layers. Instead, if there is local entrainment or detrainment or net transport through the lateral boundaries within a layer, the net mass flux from these processes is instantaneously balanced by domainwide vertical mixing, distributed according to the weight function  $W_k(\phi, \theta)$ . The mixing velocity,  $\omega_k$ , in hydromixing is relatively simple and depends only on the net mass flux just described; the layer thickness; a reference vertical mixing velocity,  $\tilde{\omega}_k$ ; a layer thickness at which to start entrainment,  $h_k^+$ ; a layer thickness at which to start detrainment,  $h_k^-$  (typically deactivated by setting to a large value); and the weight function,  $W_k(\phi, \theta)$ . In the simulations for this study,  $W_k = 1$ , a uniform distribution, although more sophisticated forms have been used in global versions of the NLOM with considerable success (Shriver and Hurlburt 1997).

Hydromixing is an important aspect of the NLOM design since it allows layers to outcrop via interface ventilation. However, this design and restricting the bottom topography to the lowest layer also enhances model efficiency because positive layer thickness is maintained for all layers everywhere, a requirement for the modal decomposition used in the semi-implicitization of external and internal gravity waves. From a dynamical point of view, once a layer has reached the thickness of  $h_k^+$ , it is dynamically inactive over the outcropped region in the sense that the resulting uniformly thick layer can no longer contribute to a pressure gradient. The impact of isopycnal outcropping on the circulation in the JES is discussed in more detail in section 5.

The NLOM has been used to investigate ocean dynamics in both regional and global models. Hurlburt et al. (1996) performed a series of simulations of the Pacific Ocean, including the JES, which demonstrated the importance of baroclinic instability and realistic bottom topography for simulating the Kuroshio/Oyashio and Kuroshio Extension. Most of their simulations included six active layers with a relatively thick surface layer (135 m). That layer structure was optimal for the Pacific Ocean because it allowed the formation of a realistic equatorial undercurrent, but was too thick in the JES to permit the formation of a robust NB via interface ventilation (Hurlburt et al. 1996). In addition, the horizontal grid resolution ( $1/8^\circ$ , or about 14 km) was apparently too coarse to achieve the upper ocean–topographical coupling needed for realistic separation of the EKWC, although that resolution was sufficient for the coupling mechanism to occur in the region of the Kuroshio. Hurlburt and Metzger (1998) reported that  $1/16^\circ$  resolution

was required to simulate the bifurcation of the Kuroshio at the Shatsky Rise by way of upper ocean–topographical coupling. They found that this coupling via baroclinic instability and particular features of the Shatsky Rise topographic complex were essential to the bifurcation and the existence of the northward branch even though the simulated Kuroshio never directly impinged on the topography. Of particular interest to this study is to determine whether the upper ocean–topographical coupling described in Hurlburt et al. (1996) and Hurlburt and Metzger (1998) can affect the separation latitude of the EKWC and other features of current systems in the JES, which is characterized by a significantly different flow regime with volume transports typically an order of magnitude less than those observed in the Kuroshio.

Others have used layered models in the JES with some success. Seung and Kim (1997) used a version of the Miami Isopycnal Coordinate Ocean Model (Bleck et al. 1992) to investigate the renewal time of the upper intermediate water. Their results indicated particularly strong mixing and isopycnal outcropping offshore from the Siberian coast during winter. These results were in agreement with those of Seung (1997), who applied the ventilation theory developed by Luyten et al. (1983) to the JES. Seung and Kim (1995) used a 2.5-layer, reduced-gravity model that included throughflow forcing and/or analytic wind stress curl. When buoyancy flux via a mixed layer was included, the intermediate layer outcropped north of the polar front, causing cyclonic circulation in that region and southward displacement of the separation latitude of the EKWC. Vasilev and Makashin (1992) developed a transport streamfunction model to show the impact of deep convection on the ventilation of deep water in the northern JES.

### 3. Design of the model simulations

Implementing the NLOM for the JES region was relatively straightforward. The model domain extends from  $34.25^\circ$  to  $49^\circ\text{N}$ . The model domain and bottom topography are shown in Fig. 1. Unvaried model parameters are given in Table 1. Several simulations were performed to determine the minimum number of layers to include and to determine the sensitivity of the model solutions to various combinations of layer thickness. These results (not shown) demonstrated the need for at least four layers, with interface depths of 60 m, 135 m, and 250 m, respectively (Table 1). The relatively thin top layer (60 m) allows isopycnal outcropping via interface ventilation to occur over much of the basin, which, as discussed in section 5, is critical for robust simulation of the NB along the coast of Honshu. The depth of the second interface (135 m) is chosen to coincide with the approximate sill depths of the inflow/outflow straits, and also plays a role in the dynamics associated with isopycnal outcropping. The depth of the third interface (250 m) approximates the mean depth of the thermocline which separates the

TABLE 1. Unvaried model parameters.

Parameter	Value(s)	Definition
$C_b$	$2 \times 10^{-3}$	Bottom drag coefficient
$C_k$	0	$k$ th interfacial stress coefficient
$C_m$	1	Coefficient of additional interfacial friction associated with entrainment
$g$	$9.8 \text{ m s}^{-2}$	Acceleration due to gravity
$h_k^+$	50 m ( $k = 1$ ) 40 m ( $k = 2, 3$ )	Thickness of layer $k$ at which entrainment starts
$h_k^-$	Deactivated	Thickness of layer $k$ at which detrainment starts (deactivated by making very large)
$\rho_{k+1} - \rho_k$	0.8/0.32/0.42 $\text{kg m}^{-3}$	Stratification between layers $k$ and $k + 1$
$\sum_{i=1}^k H_i$	60/135/250/bottom (m)	Mean depth at the bottom of layer $k$
$\tilde{\omega}_k$	0.04 $\text{cm s}^{-1}$	$k$ th interface reference vertical mixing velocity

warm saline surface waters from the cool homogeneous deep water. In the context of water masses, the top three layers approximate the location of the surface and intermediate water, while the abyssal layer represents the Japan Sea Proper Water. The maximum depth in the model domain is 3750 m.

Communication with the Pacific Ocean occurs via inflow through Tsushima Strait and outflow through the Tsugaru and Soya Straits at the model boundaries. A review of the literature (see Preller and Hogan 1998) indicates significant variability in the distribution and amplitude of flow through the straits (e.g., Miyazaki 1952; Yi 1966; Toba et al. 1982). Here, inflow through Tsushima Strait is divided into two separate inflow ports, one each for the western and eastern channels of Tsushima Strait. The mean volume transport of the *total* inflow is 2.0 Sv ( $\text{Sv} \equiv 10^6 \text{ m}^3 \text{ s}^{-1}$ ), but a seasonal signal is superimposed such that the maximum inflow and outflow of 2.66 Sv occurs in July and the minimum of 1.34 Sv occurs in January (33% peak deviation from the mean). At any given time the inflow is segmented so that 75% enters through the western channel and 25% through the eastern channel. Vertically, two-thirds of the total inflow (for both channels) enters the basin through layer 1, while the remaining one-third enters through layer 2. The straits are closed in layers 3 and 4. Inflow through Tsushima Strait is instantaneously and exactly balanced by outflow through the Tsugaru and Soya Straits (the Tartar Strait is neglected) using a modified Orlanski (1976) boundary condition. The outflow is distributed such that two-thirds of the flow exits through Tsugaru Strait and the remaining one-third through Soya Strait. The vertical distribution for the outflow is the same as for the inflow ( $\frac{2}{3}$  exits through layer 1,  $\frac{1}{3}$  through layer 2). These boundary conditions are not based on any single observation or dynamical

calculation, but instead represent a compromise for the wide range of limited observations cited in the literature.

A modified version of the  $\frac{1}{12}^\circ$  ETOP05 bottom topography (National Oceanic and Atmospheric Administration 1986) was used to represent the coastline geometry and bottom topography. The maximum depth was set to 3750 m and the minimum depth at 200 m (near the shelf break). As such, the 200-m isobath was used as the model boundary. For the JES, this is a reasonable first approximation as much of the basin is characterized by narrow continental shelf regions, and shelf dynamics are quite different than those in deep water. The ETOP05 bottom topography was first interpolated to  $\frac{1}{32}^\circ$ , then modified for better agreement with detailed topographic charts (Fig. 1). The  $\frac{1}{8}^\circ$  and  $\frac{1}{16}^\circ$  versions of the model geometries were formed by subsampling the  $\frac{1}{32}^\circ$  model grid, and the  $\frac{1}{64}^\circ$  model geometry was formed by interpolation from the  $\frac{1}{32}^\circ$  model grid. To reduce the generation of energy at scales that are poorly resolved by the model, the topographic depths are smoothed twice using a center-weighted nine-point real smoother.

Most of the simulations used in this study are forced with the HR monthly wind stress climatology. The individual wind stress components from this climatology have a native grid resolution of  $2.0^\circ$  and were interpolated to the various model grid resolutions with cubic spline interpolation. To dampen the presence of  $4^\circ$  wavelength noise associated with the wind stress on the original  $2^\circ$  field, the wind stress fields were smoothed once with a center-weighted nine-point real smoother. Two simulations, (8NEC and 8NEO; Table 2), were forced with a monthly mean wind stress climatology formed from the European Centre for Medium-Range Weather Forecasts 1979–93 10-m reanalysis winds (Gibson et al. 1997). Overall, the ECMWF climatology has more spatial structure and stronger wind stress and wind stress curl than the HR climatology. However, both wind sets are generally characterized by positive (negative) wind stress curl in the northern (southern) part of the JES, and both show significantly stronger wind stress during the winter months (associated with high atmospheric pressure over Siberia) relative to the summer months.

#### 4. Linear simulations

The framework for this study is to use an ensemble of simulations that systematically increases in dynamical complexity. The simplest member of this ensemble is a linear 1.5-layer, reduced-gravity (RG) model, which has one internal vertical mode and a bottom layer that is infinitely deep and at rest. As such, it includes only the lowest order dynamics. Furthermore, it reveals the deterministic ocean model response to external forcing and provides a baseline comparison for other simulations, which have added features like nonlinearity, bottom topography, multiple vertical modes, flow instabilities, and isopycnal outcropping. Figure 3 shows the mean sea surface height (SSH) from three 1.5-layer,

TABLE 2. List of simulations.

Simulation	Resolution	Model layers	$A$ ( $\text{m}^2 \text{s}^{-1}$ )	Wind forcing	Generic description
8LHO	$1/8^\circ \times 45/256^\circ$	1.5	50	HR	Linear RG HR winds only
8LPO	$1/8^\circ \times 45/256^\circ$	1.5	50	HR	Linear RG ports only
8LHP	$1/8^\circ \times 45/256^\circ$	1.5	50	HR	Linear RG ports and HR winds
8NHO	$1/8^\circ \times 45/256^\circ$	4.0	50	HR	Nonlinear HR winds only
8NEO	$1/8^\circ \times 45/256^\circ$	4.0	50	ECMWF	Nonlinear ECMWF winds only
8NPO	$1/8^\circ \times 45/256^\circ$	4.0	50	HR	Nonlinear ports only
8NHP	$1/8^\circ \times 45/256^\circ$	4.0	50	HR	Nonlinear ports and HR winds
8NHP3	$1/8^\circ \times 45/256^\circ$	3.0	50	HR	As above with three active layers
8NEP	$1/8^\circ \times 45/256^\circ$	4.0	50	ECMWF	Nonlinear ports and ECMWF winds
8NFB	$1/8^\circ \times 45/256^\circ$	4.0	50	HR	Flat bottom version of 8NHP
8NRG	$1/8^\circ \times 45/256^\circ$	3.5	50	HR	RG version of 8NHP
16NHP	$1/16^\circ \times 45/512^\circ$	4.0	15	HR	$1/16^\circ$ analog of 8NHP
32NHP	$1/32^\circ \times 45/1024^\circ$	4.0	5	HR	$1/32^\circ$ analog of 8NHP
32NHPb	$1/32^\circ \times 45/1024^\circ$	4.0	5	HR	32NHP with modified topography
32NFB	$1/32^\circ \times 45/1024^\circ$	4.0	5	HR	Flat bottom version of 32NHP
32NRG	$1/32^\circ \times 45/1024^\circ$	3.5	5	HR	RG version of 32NHP
64NHP	$1/64^\circ \times 45/2048^\circ$	4.0	2	HR	$1/64^\circ$ analog of 8NHP

reduced-gravity simulations that differ only in the type of external forcing applied. For these simulations, linearity was achieved by reducing the amplitude of the wind and/or throughflow forcing by a factor of  $10^3$ . The result is very small local time derivatives, small nonlinear advective terms, and small amplitude variations in the interface depth. Dynamically, the linear solutions in Fig. 3 are essentially the same as Munk (1950) with a Sverdrup (1947) interior calculated using realistic wind and/or throughflow forcing and coastline geometry, except that horizontal friction is applied everywhere and the SSH field includes a component that balances the wind stress but contributes nothing to the velocity field. However, this component does allow departures from  $\text{SSH} = \text{const}$  along the boundary where

there is no flow through the boundary. These are evident, but small in Fig. 3b.

The mean SSH from simulation 8LPO (Table 2), which was driven by seasonally varying throughflow forcing (only) is examined (Fig. 3a). It is uncommon to consider a “port-driven” solution in the context of Sverdrup dynamics, but this simulation simply shows the impact of flow through the JES in a linear fashion, and depicts the TWC as a Munk ( $\beta^{1/3}$ ) boundary layer that hugs the western boundary until it is forced to separate from the coast of Korea and flow eastward to satisfy the constraints of the outflow ports. Consistent with the distribution of the outflow ports (described in section 3), about two-thirds of the flow separates at the latitude of the Tsugaru outflow port, and the remaining one-third

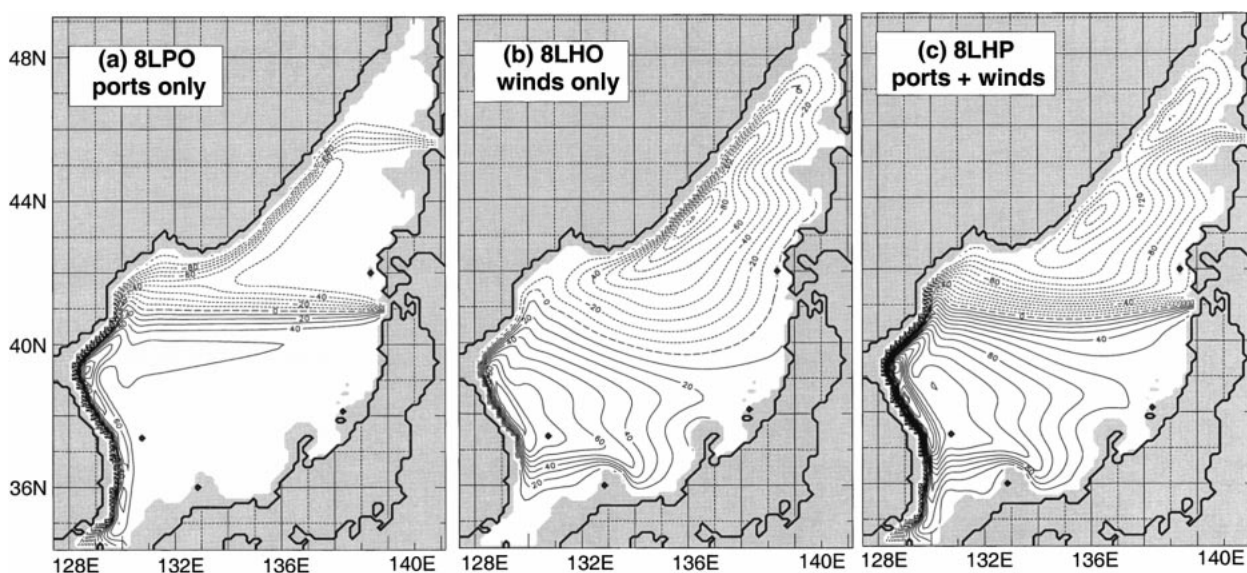


FIG. 3. Mean SSH from  $1/8^\circ$  1.5-layer reduced-gravity linear simulations forced by (a) seasonally varying throughflow (8LPO), (b) monthly HR winds (8LHO), and (c) both throughflow and HR winds (8LHP). Linearity was achieved by reducing the amplitude of the external forcing by  $10^3$ . For plotting, the SSH has been scaled upward by the same factor. Contour interval is 1 cm.



separates at the latitude of the Soya outflow port. The northeastward flow along the Siberian coast (Fig. 3a) is needed to satisfy the constraint of the Soya outflow port. This is contrary to the observed cyclonic circulation in the northern part of the JES and in particular with the observed southwestward flow along the Siberian coast associated with the LCC (Fig. 2). This also results in a severe overshoot of the EKWC, which is observed to separate from the coast at about 37°–38°N. Indeed, “overshooting” of boundary currents has been a problem with previous modeling efforts in the JES, particularly those with relatively coarse horizontal grid resolution (e.g., Seung and Kim 1993).

The mean SSH from simulation 8LHO, which was forced with the HR monthly wind stress climatology (only), is shown in Fig. 3b (Table 2). This solution is characterized by two large gyre systems, an anticyclonic gyre in the southern half of the basin associated with negative wind stress curl and a cyclonic gyre in the northern half basin associated with positive wind stress curl. Unlike simulation 8LPO, this solution has realistic (in terms of the flow direction) southwestward flow along the Siberian coast. Similar to simulation 8LPO, the 8LHO simulation has a northward Munk  $\beta^{1/3}$  boundary current on the western side of the anticyclonic gyre in the southern part of the basin. This Munk boundary layer also hugs the coast up to about 41.5°N, but here the separation is controlled by the overall pattern of the wind stress curl, and the boundary between the two gyres is approximately the location of the zero wind stress curl line. The anticyclonic gyre in the southern part of the basin results in unrealistic southwestward flow along the coast of Honshu. Hence, in the linear sense, the HR climatology acts counter to realistic northeastward flow along the coast of Honshu associated with the NB of the TWC (Fig. 2).

When the linear solution is forced with both winds and ports, as in simulation 8LHP (Fig. 3c), the result is a linear superposition of simulations 8LPO and 8LHO, and in any given region the solution is altered depending on which of the individually forced solutions dominates. For instance, in the area off the Siberian coast, simulation 8LHP shows southwestward flow because the southwestward flow from simulation 8LHO is stronger than the northeastward flow that resulted from simulation 8LPO. The net result is realistic flow to the southwest, which is the model’s representation of the LCC. This result suggests that the LCC is a predominantly wind-driven current. Although simulation 8LHP shows an unrealistic latitude for the EKWC separation and a southwestward boundary current along the coast of Honshu, it is noteworthy that the rudiments of most of the basic current systems are present in a solution that (only) contains the lowest order dynamics. In particular, simulation 8LHP shows a cyclonic (anticyclonic) gyre in the northern (southern) part of the basin, a polar front separating the two gyres, the southward flowing LCC, and the EKWC. However, the NB of the TWC, a major

current in the JES, is totally absent and the large overshoot of the EKWC beyond its observed separation latitude means the NKCC is absent as well.

In the following sections, the dynamical complexity of the simulations is systematically increased by including some combination of nonlinearity, multiple internal modes, realistic bottom topography, isopycnal outcropping, and flow instabilities. This modular approach to investigating the dynamics provides a road map for identifying the crucial processes needed to simulate the JES circulation in a robust and realistic fashion and the major changes needed to correct the deficiencies seen in the linear solutions.

### 5. Impact of nonlinearity, external forcing, and isopycnal outcropping

The linear simulations discussed in the previous section demonstrated that most of the large-scale circulation features in the JES can be reproduced with minimal dynamical ingredients when the model includes throughflow and wind forcing. A major exception is unrealistic southwestward flow along the coast of Honshu due to the wind stress curl in the HR climatology. In the following sections, the model complexity is progressively increased by adding nonlinearity, bottom topography, multiple internal modes (i.e., more layers), interface ventilation, and diapycnal mixing. The model sensitivity to external forcing is also examined. The dynamical consequences of these changes, which can be examined in a systematic fashion, include the possibility of barotropic and baroclinic flow instabilities, the formation of inertial jets and boundary layers, and isopycnal outcropping.

As in the previous section, we begin by investigating the impact of the external forcings, individually and collectively, but here using a series of nonlinear simulations. The mean SSH and surface layer currents from a sequence of 4-layer,  $1/8^\circ$  simulations forced with seasonal throughflow and/or HR monthly winds are examined (Fig. 4). In addition to nonlinearity, these simulations include multiple internal baroclinic modes and realistic bottom topography. The addition of these dynamical ingredients results in  $O(1)$  changes from the linear solutions, providing much more realistic depictions of the current systems. Even when driven by seasonal throughflow forcing only (simulation 8NPO), most of the major surface layer currents, nonlinear recirculation gyres, and realistic mesoscale circulation features occur throughout the JES (Fig. 4a). In contrast to the linear simulations, the currents are inertial in character and the fronts meander, forming rings and eddies. For instance, in simulation 8NPO, the EKWC flows northward along the Korean coast until it separates from the coast near 41°N, which is farther north than the observed separation latitude. However, unlike simulation 8LPO, after separation from the coast the EKWC forms a large meander before flowing southward and

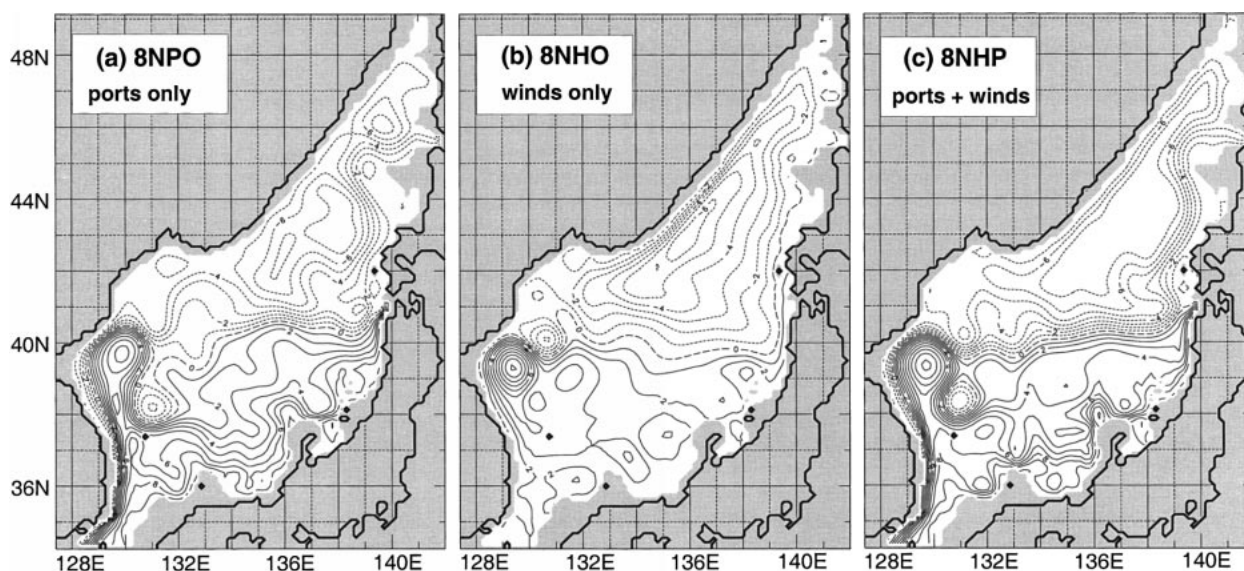


FIG. 4. Mean SSH from 4-layer  $\frac{1}{8}^\circ$  nonlinear simulations forced by (a) seasonally varying throughflow (8NPO), (b) HR monthly climatological winds (8NHO), and (c) both throughflow and HR winds (8NHP). Contour interval is 1 cm.

bifurcating into two distinct branches (Fig. 4a). The northern branch joins the eastward flow along  $40^\circ\text{N}$  contributing to the polar front, while the other branch joins the NB, which flows along the coast of Honshu. The latter current is totally absent in linear simulation 8LPO. In the northern part of the JES the currents are characterized by overall cyclonic circulation, even in the absence of wind forcing. Some of the flow from this gyre exits to the Pacific Ocean via Soya Strait, while the remainder forms a nonlinear recirculation gyre, including the LCC along the Siberian coast even though wind forcing is absent.

Simulation 8NHO is identical to simulation 8NPO except that it is forced by the HR monthly wind stress climatology (only). Again, the impact of nonlinearity is evident. The mean SSH and surface layer currents (Fig. 4b) are characterized by cyclonic circulation in the northern part of the basin and anticyclonic circulation in the southern part, although flow along the coast of Honshu is quite weak and unrealistically southwestward west of the Noto Peninsula. The polar front, which is also weak, marks the boundary between the two gyres. The cyclonic gyre in the northern part of the basin is associated with positive wind stress curl, which produces isopycnal outcropping and locally intense open ocean upwelling due to Ekman suction offshore from the Siberian coast.

When both seasonal throughflow and wind forcing are included, as in simulation 8NHP (Fig. 4c), the impact of each forcing mechanism is visible in Fig. 4. As evidenced by the similarity of Figs. 4a and 4c, the seasonal throughflow forcing clearly dominates the modeled circulation, particularly the meandering and bifurcation associated with the EKWC. However, the wind-driven component clearly strengthens the northern gyre

and the flow along the polar front and it affects the shape of the eddy that forms where the EKWC separates from the Korean coast. Except for the separation latitude of the EKWC, which is farther to the north than observed, simulation 8NHP reasonably replicates all of the major current systems depicted in Fig. 2. Perhaps the single largest improvement in simulations 8NPO and 8NHP is the formation of the NB of the TWC along the coast of Honshu, which was either missing (simulation 8LPO) or flowing in the wrong direction (simulations 8LHO and 8LHP) in the linear solutions. Using a simplified model with port and wind forcing, Yoon (1982) attributed the formation and persistence of the NB to topographical control. This hypothesis was supported in numerical studies by Kawabe (1982) and Ichiye (1984). In the simulations described here, a different mechanism is offered as an alternative explanation for the formation of this boundary current.

In these simulations isopycnal outcropping is the key dynamical mechanism responsible for the formation of the NB of the TWC. In regions of outcropping, the model interfaces ventilate via strong diapycnal mixing, a process described in section 2. Isopycnal outcropping and ventilation can occur in response to mechanisms such as (i) Ekman suction, (ii) coastal upwelling in response to longshore winds or Kelvin wave propagation, (iii) geostrophic response of an interface to a current (the mechanism for isopycnal outcropping north of the polar front in simulation 8NPO, a simulation with no wind forcing), or (iv) formation of a cyclonic eddy. In general, interface ventilation in the NLOM is a consequence of having  $O(1)$  variations in layer thickness and is enhanced by including a relatively thin top layer in the model (see Table 1). These conditions permit the thin top layer (60-m mean depth in these simulations)

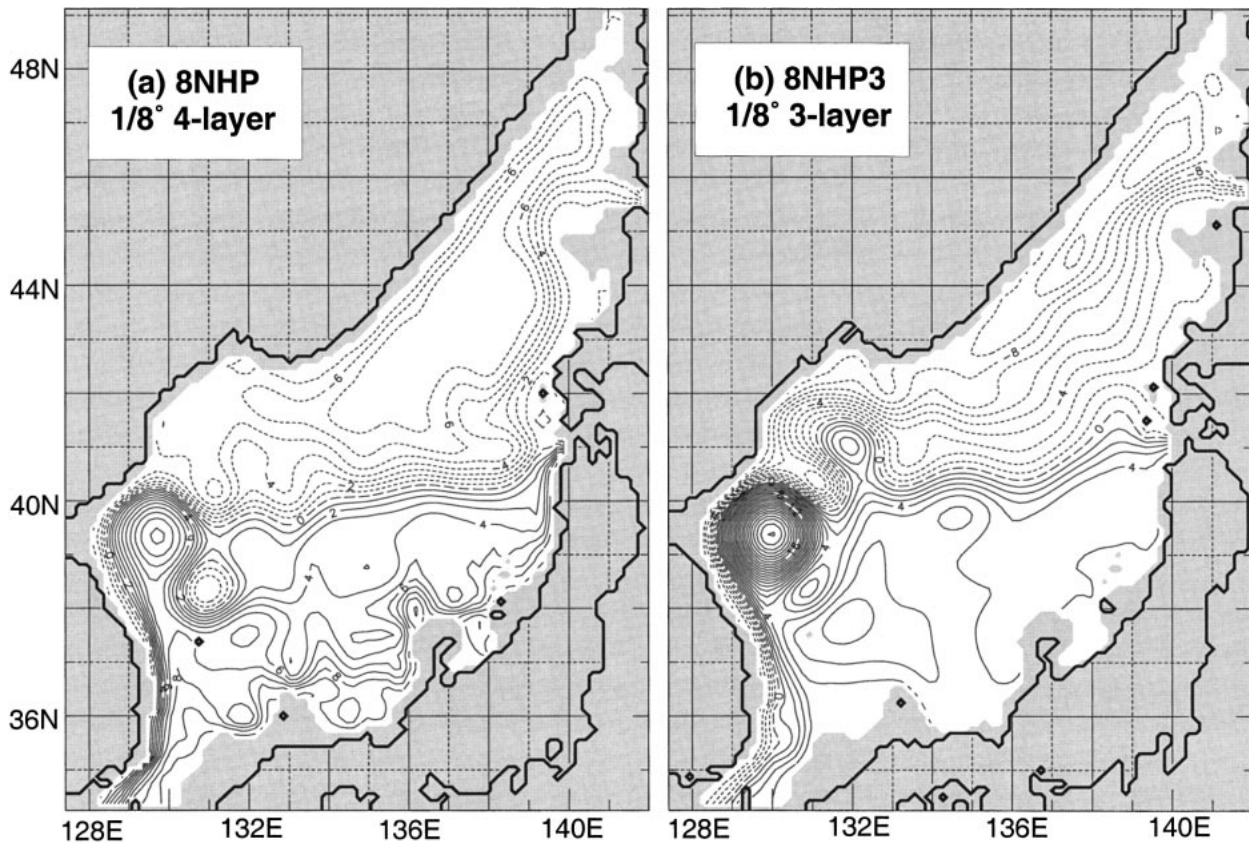


FIG. 5. Mean SSH from  $1/8^\circ$  nonlinear simulations forced by HR monthly climatological winds and seasonally varying throughflow for (a) 4-layer case ( $H_1 = 60$  m) and (b) 3-layer case where the top two layers from (a) have been combined ( $H_1 = 135$  m). The removal of the thin top layer in (b) inhibits isopycnal outcropping and hence the formation of the Nearshore Branch along the coast of Honshu. Contour interval is 1 cm.

to outcrop over much of the basin for most of the time. In simulations without a thin top layer, such as simulation 8NHP3 (Table 2), the NB is nonexistent, and flow south of the polar front is weakly anticyclonic (Fig. 5). This anticyclonic flow is similar to the flow depicted in the linear solutions that included wind forcing (e.g., Figs. 3b,c). In simulation 8NHP (Figs. 4c and 5a), however, the NB is a well-defined boundary current along the entire coast of Honshu. The meridional segments of this current remain as eastern boundary currents in the mean (rather than propagating westward as nondispersive Rossby waves) because the vertical mixing term is larger in magnitude than the mass divergence term in the continuity equation [Eq. (3)]. Restated, this means that the rate of upward vertical mixing in the region of outcropping is faster than the rate of interface deepening produced by westward Rossby wave propagation. Fundamentally, this is an extreme example of the geostrophic current mechanism for outcropping (“iii” above), which occurs because there is a surface layer that has insufficient volume to carry the portion of the TWC transport within that layer, unless it is confined near the southeastern boundary between the Tsushima and Tsugaru Straits. This is discussed further shortly.

Consistent with this explanation and the wind forcing, the flow immediately below in layer 2 (which does not outcrop in this region) is in the opposite direction. In contrast, Kim and Yoon (1994) used a multilevel model with  $1/6^\circ$  resolution to describe the seasonal variability of the NB, and reported that it drifted offshore due to the  $\beta$  effect and developed into a meandering phase from summer to autumn.

From section 2, the outcropped layers do not attain zero-layer thickness, but rather outcrop to a specified layer thickness that controls activation of vertical mixing. In the JES, this depth (50 m) is chosen to be a nominal mixed layer depth for layer 1. The result, however, is that layers with an outcropped bottom interface are baroclinically inactive (i.e., do not contribute to the pressure gradient) because they are isopycnal and have minimal variation in layer thickness in outcropped regions. The interface ventilation for simulations 8NPO, 8NHO, and 8NHP is examined using maps of the fraction of time that each interface ventilates (Fig. 6). From Fig. 6a, the top interface from simulation 8NPO ventilates over 90% of the time north of the polar front. Simulation 8NHO (Fig. 6b) on the other hand, produces much less interface ventilation except in a small region

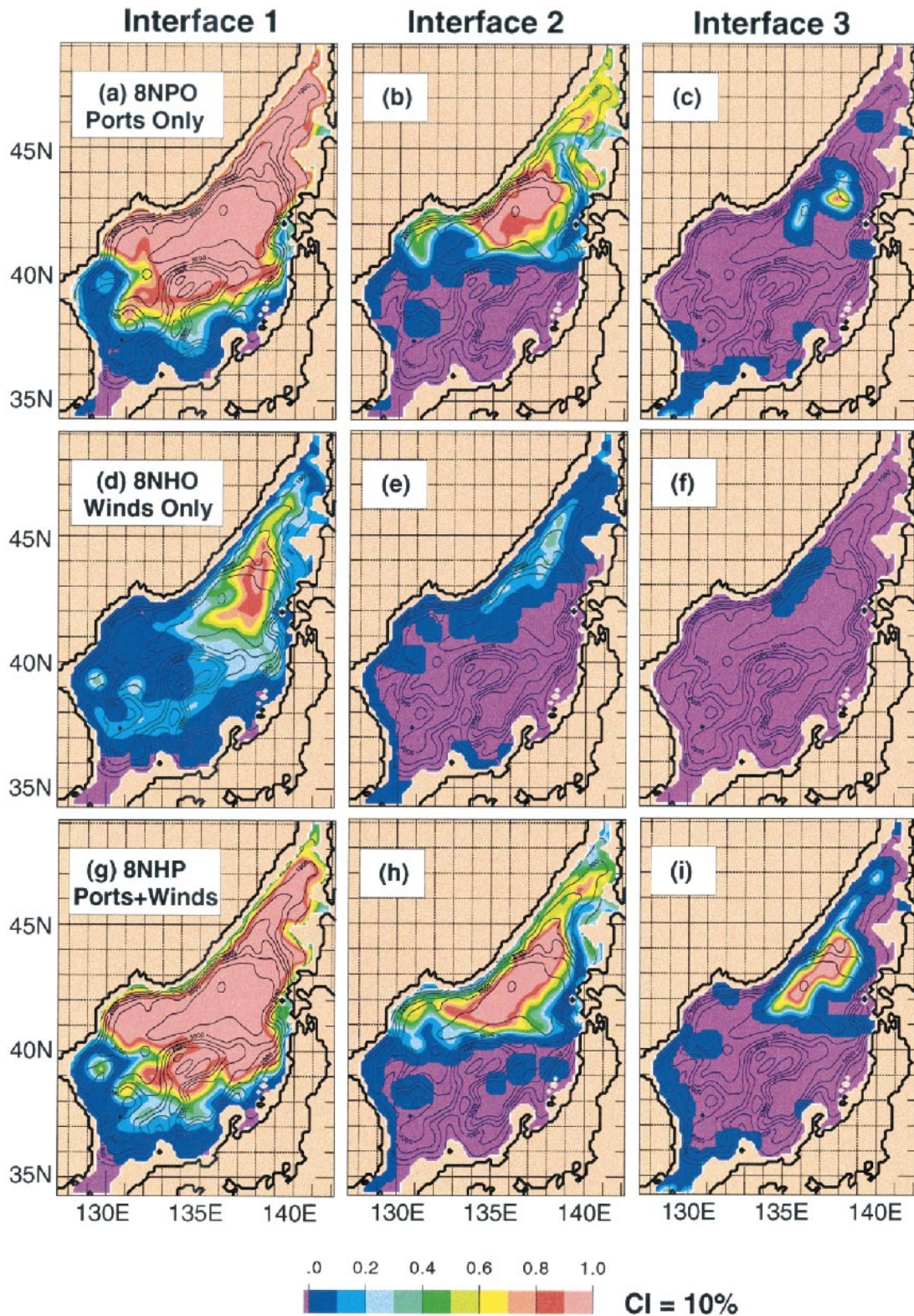


FIG. 6. Maps of the percent of time that an interface ventilates from 4-layer  $\frac{1}{8}^\circ$  nonlinear simulations. (a–c) show interfaces (1–3) for throughflow forced simulation (8NPO); (d–f) show interfaces (1–3) for HR wind forced simulation (8NHO), and (g–i) show interfaces (1–3) for simulation forced by both throughflow and winds (8NHP). Units are percent of time; contour interval is 10%. Note 0% is a separate color.

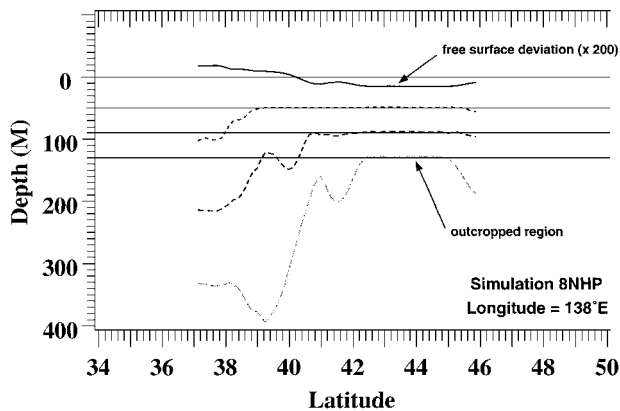


FIG. 7. Meridional cross section of mean interface depth along  $138^{\circ}\text{E}$  from 4-layer,  $\frac{1}{8}^{\circ}$  simulation forced by both winds and ports (8NHP). The horizontal lines at depths 50 m, 90 m, and 130 m indicate the cumulative depths of the  $h_i^+$  (Table 1). For the thickness of a given layer, vertical mixing is turned on when  $h_i \leq h_i^+$ .

in the central subpolar gyre. For a given simulation, the effect of outcropping due to the external forcing is cumulative over all layers, and that is reflected in the interface ventilation maps for simulation 8NHP (Figs. 6g–i).

By measuring the net mass flux across each interface, the strength of the mean meridional overturning cell in simulation 8NHP is determined to be about 1.7 Sv over the entire basin. Of that, 0.36 Sv of exchange occurs with the abyssal layer. This exchange rate gives a residence time for renewal of the deep water of about 130 years, close to that estimated by Kim and Kim (1997) and Seung and Kim (1997). As Fig. 6i indicates, nearly all of the abyssal layer outcropping occurs in the northwestern part of the basin, where the third interface is ventilated over 90% of the time. Previous studies (Senjyu and Sudo 1994; Seung and Yoon 1995a) indicate that this is a likely area for deep convection, and that this convection produces cyclonic circulation of the intermediate and deep water north of the polar front, an indication which is also supported by numerical studies (Seung and Kim 1993; Seung and Yoon 1995b).

To rephrase an earlier statement, the uniformly thin outcropped layers contribute very little to the pressure gradient and are dynamically inactive in that sense. As such, a robust current (the NB) persists in the region where the thin top layer is *not outcropping*, and although the pressure gradient in layer 1 is due to the gradients of layer thickness anomaly in all four layers, the gradients in layer 1 are essential for the formation of the NB, and the flow is reversed in layers below the surface layer as in the wind-forced contribution. The mean layer structure can be depicted in meridional cross sections of interface depth. One cross section (Fig. 7), for simulation 8NHP along  $138^{\circ}\text{E}$ , demonstrates that the top interface in simulation 8NHP does not ventilate south of  $39^{\circ}\text{N}$ , the location of the NB. Likewise, the second interface ventilates along the polar front at about  $40.5^{\circ}\text{N}$ .

Finally, where all three interfaces ventilate, between about  $42.5^{\circ}$ – $45^{\circ}\text{N}$  along  $138^{\circ}\text{E}$  (Figs. 6i and 7), there is no contribution to the pressure gradient except from the barotropic mode. Hence, the mean SSH shows little variation there (Fig. 4c), and the current velocities are weak (although current transports can be large because the flow is barotropic).

Analysis of the simulations in Fig. 4 revealed the impact of the wind-driven circulation in the JES when HR monthly winds are used. However, different wind forcing can produce greatly different results, particularly with respect to separation of the EKWC. For example, Kim and Yoon (1996) achieved realistic separation of the EKWC in a 1.5-layer, reduced-gravity model. In that study the overshoot problem was diminished by using the Na et al. (1992) wind stress, which is characterized by strong positive wind stress curl over the subpolar gyre. The strong positive wind stress curl resulted in strengthening of the subpolar gyre, thereby moving the separation latitude of the EKWC to the south. To assess the impact that a different wind climatology has on the NLOM, two simulations (8NEO and 8NEP) were forced by a monthly wind stress climatology formed from the 1979–1993 ECMWF 10-m reanalysis winds (see section 3). Except for the wind forcing, these simulations are identical to simulations 8NHO and 8NHP (Table 2).

The mean SSH from simulation 8NEO (Fig. 8b) is significantly different than the mean SSH from simulation 8NHO (Fig. 4b). Most striking is the large anticyclonic gyre in the center of the basin. Another significant difference is the continuation of the southward flow associated with the subpolar gyre south of  $42^{\circ}\text{N}$ . In essence, this simulation contains a well-defined NKCC as well as the LCC. The NKCC flows southward to about  $37.5^{\circ}$ , where it separates from the coast, and flows eastward forming part of a large-scale cyclonic circulation that encompasses most of the basin, including northeastward flow along much of the coast of Honshu. That the separation of the NKCC occurs near the same latitude as the observed separation latitude of the EKWC is significant because it demonstrates that realistic separation of the EKWC at  $\frac{1}{8}^{\circ}$  resolution may be substantially influenced by the wind-driven circulation.

When the model is forced with seasonal throughflow and the ECMWF monthly wind stress climatology (simulation 8NEP), the separation latitude of the EKWC is much more realistic (Fig. 8c) than its HR counterpart (simulation 8NHP). In simulation 8NEP, the EKWC separates from the coast near  $37^{\circ}\text{N}$ , but the core of the current flows northward to about  $39^{\circ}\text{N}$  due to the influence of the throughflow forcing. After separation from the coast, the EKWC flows eastward along the polar front until it bifurcates into two branches in response to the large anticyclonic gyre that was observed in simulation 8NEO. The northern branch of this bifurcation flows eastward forming part of the southern boundary of the subpolar gyre. Some snapshots of the SSH (not shown) show the southern branch of the bifurcation far-

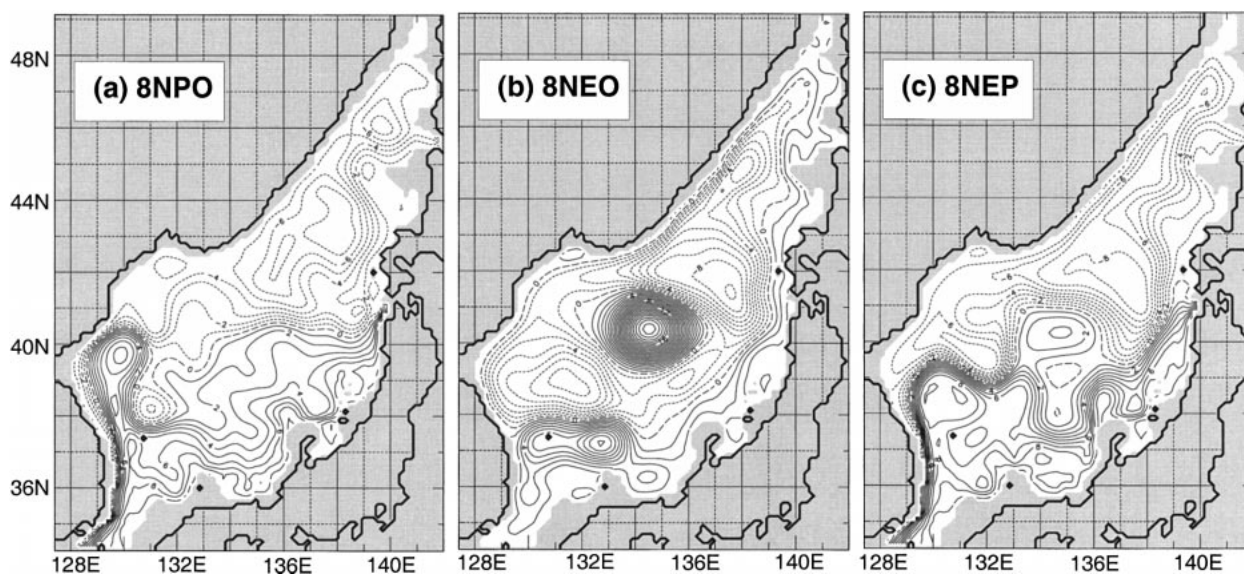


FIG. 8. Mean SSH from 4-layer  $\frac{1}{8}^\circ$  nonlinear simulations forced by (a) seasonally varying ports only (8NPO), (b) ECMWF climatological winds only (see text) (8NEO), and (c) both ports and ECMWF winds (8NEP). Contour interval is 1 cm.

ther offshore than the NB, suggesting that this branch might represent the highly variable Offshore Branch of the TWC. In these cases, the NB is fed more directly by inflow through the eastern channel of Tsushima Strait, although it tends to merge with the Offshore Branch east of  $136^\circ\text{E}$  where the continental shelf becomes very narrow and deepens considerably.

The significance of simulation 8NEP is that it clearly illustrates the model sensitivity to the atmospheric forcing, particularly with respect to separation and branching of the EKWC. It is reasonable, and indeed likely, that other wind stress climatologies give significantly different solutions than the two discussed here. However, the sensitivity of the circulation to atmospheric forcing is not the focus of this paper. Hence, in the following section, we limit our discussion to simulations forced with the HR monthly wind stress climatology, and investigate the role of horizontal grid resolution and the impact of bottom topography. Given the comparison of simulations 8NHP and 8NEP, this choice may seem counterintuitive. However, as will be shown, by purposefully choosing a wind stress climatology that is known a priori to give unrealistic results (e.g., overshoot of the EKWC), the impact of certain dynamical processes can be evaluated independent of any contribution from the atmospheric forcing, and hence, in a more clear and concise fashion.

## 6. Impact of horizontal grid resolution and bottom topography

Studies of the JES eddy field from observations have suggested a relationship between the upper ocean currents and the bottom topography (Toba et al., 1982; An et al. 1994; Lie et al. 1995). Numerical studies (Hurlburt

and Metzger 1998) show the importance of numerical model resolution on the mesoscale eddy field by demonstrating the effect of eddy variability in the Kuroshio Extension on the Kuroshio bifurcation at the Shatsky Rise. The mechanism through which the eddy field affects the mean circulation is complex, but shows that the mean flow is related to the bottom topography. Holloway (1992) introduced the concept of *topostress* as a means of parameterizing the topographic influence on circulation. Holloway et al. (1995) included this topostress parameterization in a relatively coarse resolution model of the JES, and showed that it had the effect of increasing the strength of the NKCC and of separating the EKWC close to the observed latitude. Because of NLOM efficiency, it was possible to progressively increase the horizontal grid resolution, thereby enhancing the mesoscale eddy field, to determine to what extent the mean flow, mesoscale eddy field, and bottom topography are related.

Simulations 8NHP and 64NHP form the  $\frac{1}{8}^\circ$  (14 km) and  $\frac{1}{64}^\circ$  (1.7 km) end members of a sequence of simulations that are identical except for the horizontal grid resolution and the corresponding decrease in eddy viscosity afforded by the increase in grid resolution (Table 2). Snapshots of SSH for each grid resolution (Fig. 9) and maps of mean SSH (Fig. 10) are examined. As described in section 5, the separation latitude of the EKWC in simulation 8NHP occurs farther to the north than observed. When the resolution is increased to  $\frac{1}{16}^\circ$  (simulation 16NHP, Figs. 9b and 10b), there is modest improvement in the separation latitude of the EKWC in that the current no longer hugs the Korean coastline, but there is still overshoot of the EKWC beyond  $40^\circ\text{N}$ . Also, there is a marginal increase in the number of eddies when the resolution is increased to  $\frac{1}{16}^\circ$ , particularly

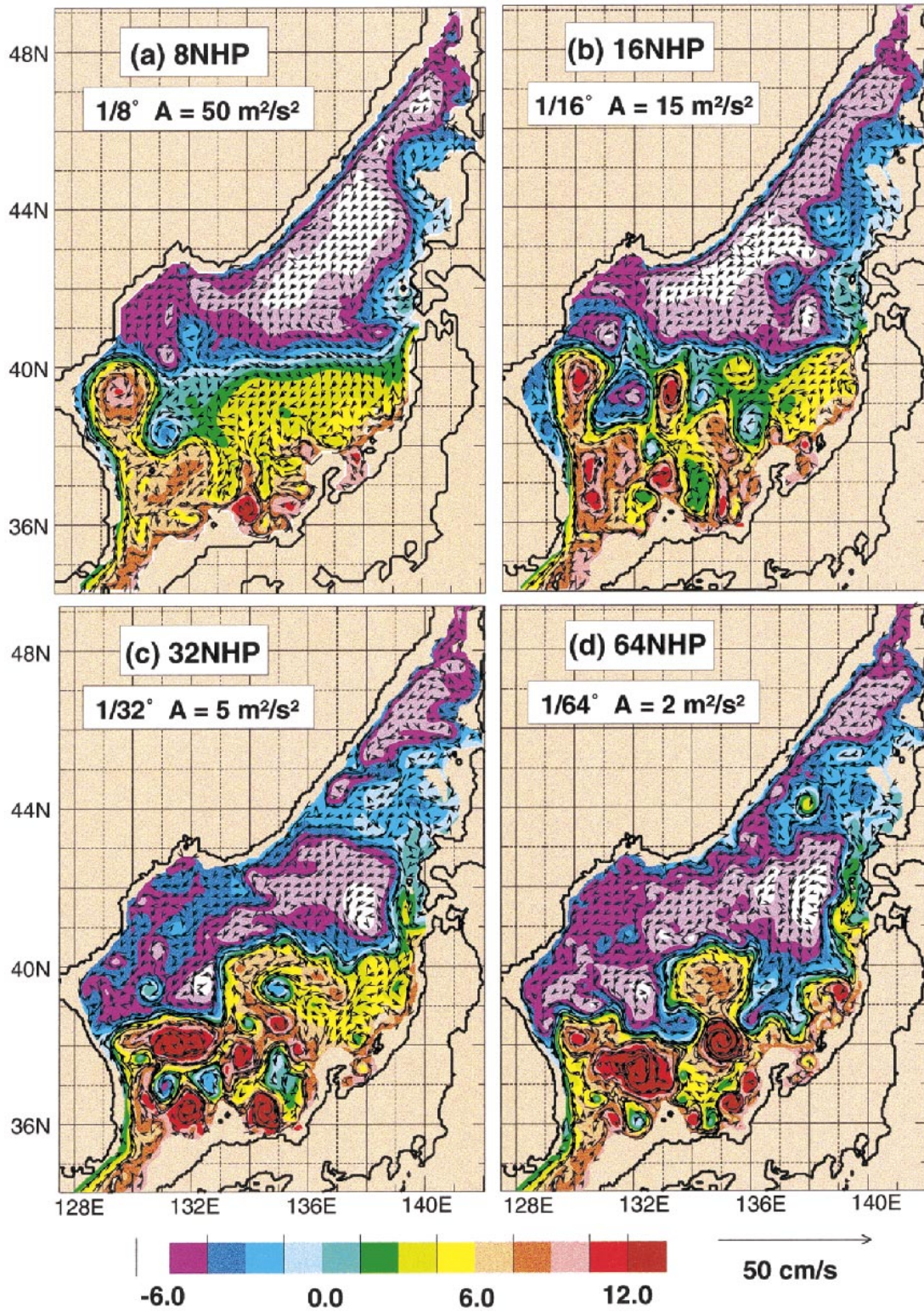


FIG. 9. Snapshots of SSH (color) and currents (vectors) on 15 Jan for 4-layer nonlinear simulations with realistic bottom topography forced by throughflow and HR winds. Resolution is (a)  $1/8^\circ$  (8NHP), (b)  $1/16^\circ$  (16NHP), (c)  $1/32^\circ$  (32NHP), and (d)  $1/64^\circ$  (64NHP). Realistic separation of the EKWC is not achieved until  $1/32^\circ$  resolution. Contour interval of SSH is 1 cm.

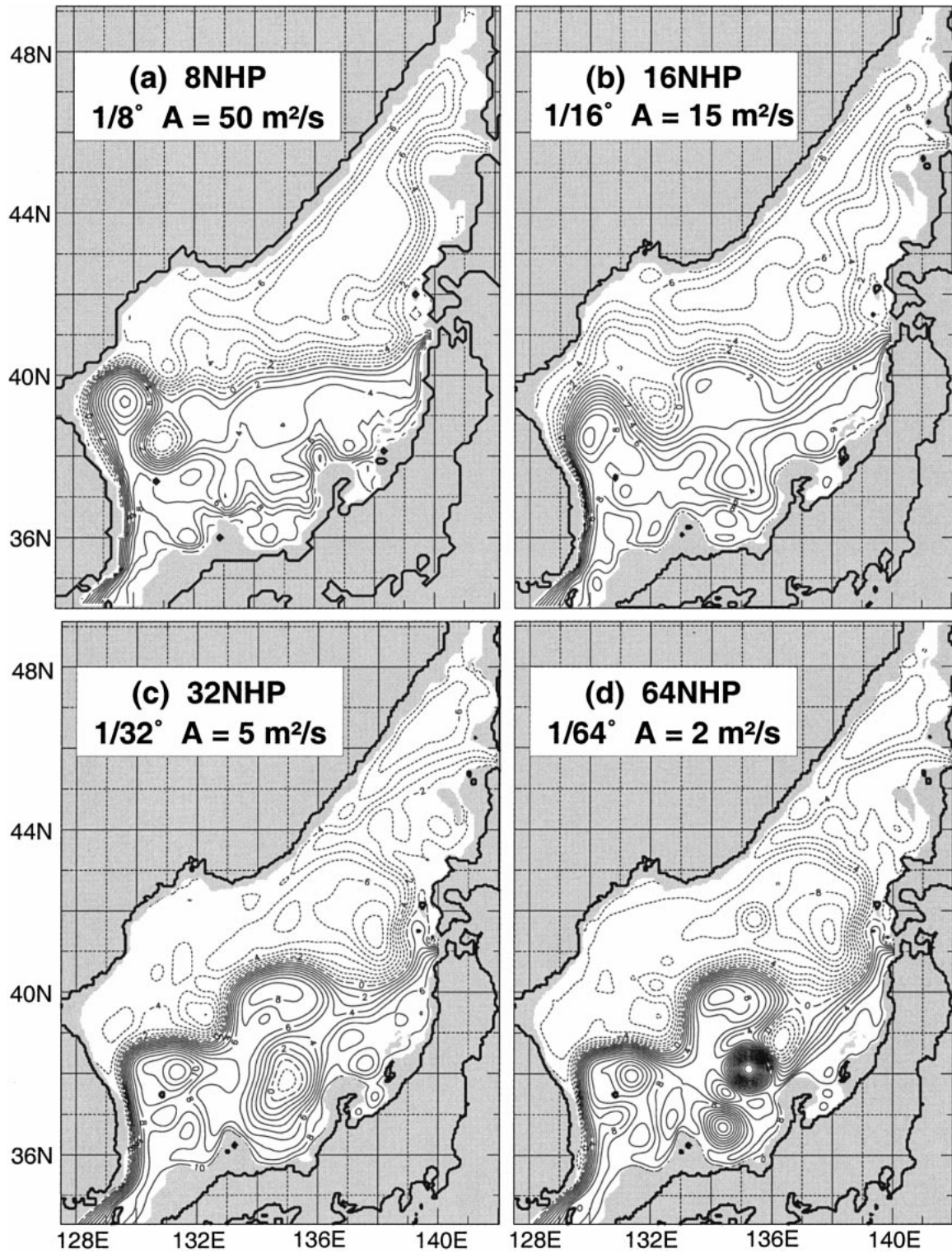


FIG. 10. Mean SSH from the same suite of simulations shown in Fig. 9. Resolution is (a)  $1/8^\circ$  (8NHP), (b)  $1/16^\circ$  (16NHP), (c)  $1/32^\circ$  (32NHP), and (d)  $1/64^\circ$  (64NHP). At least  $1/32^\circ$  resolution is required for realistic separation of the EKWC.



south of the polar front. It is not until the resolution is increased to  $\frac{1}{32}^\circ$  (simulation 32NHP, Figs. 9c and 10c) that the EKWC realistically separates at about  $38^\circ\text{N}$ . Also, the eddy field at this resolution is ubiquitous, forming predominantly warm (cold) rings on the north (south) side of the Polar Front (Fig. 9c), although the simulations at all four resolutions are eddy-resolving and demonstrate eddies in Fig. 9.

Separation of the EKWC also occurs near  $37^\circ\text{--}38^\circ\text{N}$  in simulation 64NHP (Figs. 9d and 10d). Indeed, the change in the solution when the resolution is increased from  $\frac{1}{32}^\circ$  to  $\frac{1}{64}^\circ$  is qualitatively much smaller than the change in solution that accompanies any of the other changes in grid resolution (and eddy viscosity). The largest differences appear in the region of the Yamoto Basin. In that region, simulation 32NHP is characterized by a strong cyclonic gyre but simulation 64NHP is characterized by a strong cyclonic/anticyclonic gyre pair. However, comparison of several 10-yr means (not shown) from either simulation 32NHP or 64NHP (i.e., from a single simulation) indicate that this is an area of substantial interdecadal variability, even though these simulations used climatological monthly mean forcing. This is one possible reason for the differences in this region. However, in all other regions of the JES, the fact that the mean SSH in simulations 32NHP and 64NHP is quite similar suggests that the simulation is nearly converged for mesoscale variability at  $\frac{1}{32}^\circ$  resolution.

Clearly, a profound change in the circulation dynamics has occurred between  $\frac{1}{16}^\circ$  and  $\frac{1}{32}^\circ$  resolution, particularly with respect to the separation latitude of the EKWC. What are the dynamics responsible for this fundamental change? Examination of the abyssal circulation (Fig. 11) suggests that the strength and direction of the abyssal circulation can strongly influence the surface circulation. In simulation 8NHP (Fig. 11a), the deep currents are relatively weak and are largely anticyclonic. In simulation 16NHP (Fig. 11b), localized areas of eddy-driven deep mean flows develop and are mainly associated with the topographic highs and lows. However, in simulation 32NHP (Fig. 11c), there is a profound change in the abyssal circulation compared to the coarser resolution simulations. In particular, the eddy-driven deep mean flows are much stronger and occur over most of the basin. Furthermore, there is a reversal in the current directions from anticyclonic at  $\frac{1}{8}^\circ$  resolution to cyclonic at  $\frac{1}{32}^\circ$  and  $\frac{1}{64}^\circ$  resolution. Indeed, in simulation 32NHP (Fig. 11c) there is southward abyssal flow along the coast of Korea to about  $38^\circ\text{N}$ , the observed separation latitude of the EKWC. Near  $129^\circ\text{E}$ ,  $37.5^\circ\text{N}$  the strength of the southward flowing current is  $2.4\text{ cm s}^{-1}$ , which is in close agreement with current meter measurements (Lie et al. 1989) that indicate a mean current speed of about  $3\text{ cm s}^{-1}$  in nearly the same location. With the exception of the gyres in the Yamato Basin, the strength and pathways of the mean abyssal layer currents in simulation 64NHP (Fig. 11d) are close to

those from simulation 32NHP, which is another indication that the mesoscale variability in simulation 64NHP has nearly converged with respect to that in simulation 32NHP.

In Fig. 11 we have seen the increase in the kinetic energy of the mean flow and the accompanying reversal in the direction of the abyssal circulation as the model resolution is increased from  $\frac{1}{8}^\circ$  to  $\frac{1}{32}^\circ$ . This is the result of strengthened baroclinic instability (actually a mixed baroclinic–barotropic instability) in the higher resolution simulation. Baroclinic instability is very efficient at transferring energy from the upper layers into the abyssal layer. Maps of surface and abyssal eddy kinetic energy (EKE) (Figs. 12 and 13, respectively) demonstrate how dramatically the surface and abyssal eddy energy levels increase with increasing grid resolution up to  $\frac{1}{32}^\circ$ . Those maps also show that the EKE maxima in the surface and abyssal layers are geographically collocated, a classic signature of baroclinic instability (Holland and Lin 1975).

There is a clear correlation between the unrealistic separation of the EKWC (which is accompanied by weak anticyclonic deep circulation) at  $\frac{1}{8}^\circ$  and realistic separation of the EKWC (and the reversal in the deep circulation) at resolution of  $\frac{1}{32}^\circ$  and higher. This suggests that baroclinic instability and the inclusion of realistic bottom topography are the critical factors influencing the surface circulation in the JES. Hence, to investigate the role of baroclinic instability involving the barotropic mode, it is useful to compare simulations with flat or realistic bottom topography, and reduced gravity simulations that exclude baroclinic instability involving the barotropic mode. To examine the impact of the bottom topography (or lack thereof) on the surface layer circulation, a sequence of simulations that include realistic bottom topography, a flat bottom, and a lowest layer that is infinitely deep and at rest (e.g., reduced-gravity simulations) were performed at both  $\frac{1}{8}^\circ$  and  $\frac{1}{32}^\circ$  resolution (Fig. 14; Table 2).

The circulation features and dynamics of simulation 8NHP (which included realistic bottom topography) were discussed in sections 5 and 6, but the mean SSH from that simulation is repeated (Fig. 14a) for ease of comparison. The mean SSH from reduced gravity simulation 8NRG (Fig. 14c) is strikingly similar to that from simulation 8NHP. Both show overshoot of the EKWC, a robust NB of the TWC and realistic meandering of the polar front. The presence of a robust NB in simulation 8NRG, which does not include bottom topography, is a further indication that bottom topography is not required for the formation of this current. Both also show a robust LCC off the Siberian coast. The similarity of the mean SSH from simulations 8NHP and 8NRG indicates that the bottom topography and baroclinic instability (involving the baroclinic and barotropic modes), in general, have little if any influence on the surface circulation since simulation 8NRG has a lowest layer that is infinitely deep and at rest. However, sim-

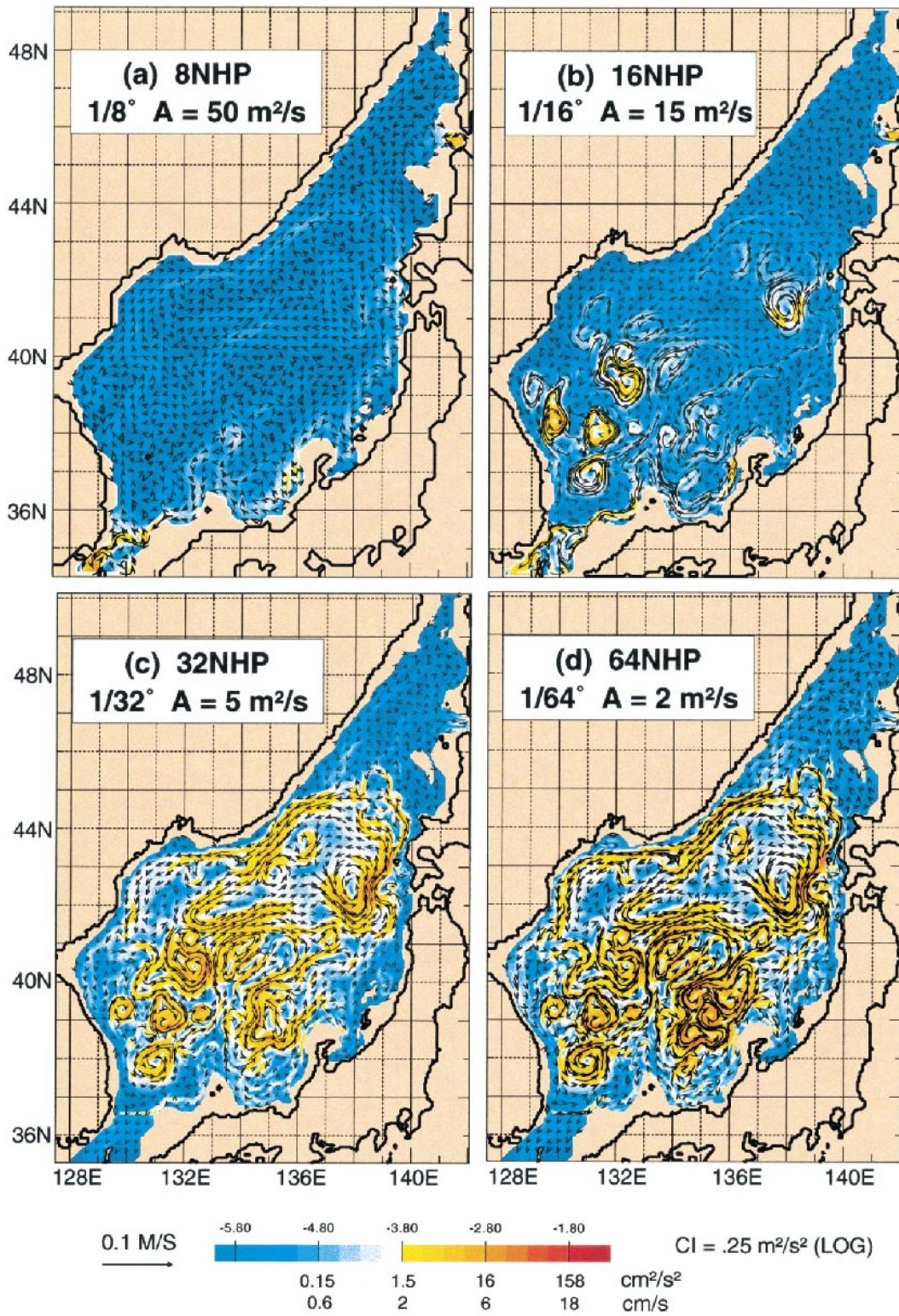


FIG. 11. Kinetic energy per unit mass of the mean abyssal flow (color) and mean abyssal currents (vectors) for the same simulations shown in Fig. 9: (a)  $\frac{1}{8}^\circ$  resolution (8NHP), (b)  $\frac{1}{16}^\circ$  resolution (16HP), (c)  $\frac{1}{32}^\circ$  resolution (32HP), and (d)  $\frac{1}{64}^\circ$  resolution (64NHP). Contour interval of KEM is  $0.25 \log_{10} \text{ m}^2 \text{ s}^{-2}$ , and is also expressed in  $\text{cm} \text{ s}^{-1}$  (mean speed) and  $\text{cm}^2 \text{ s}^{-2}$  (KEM per unit mass).

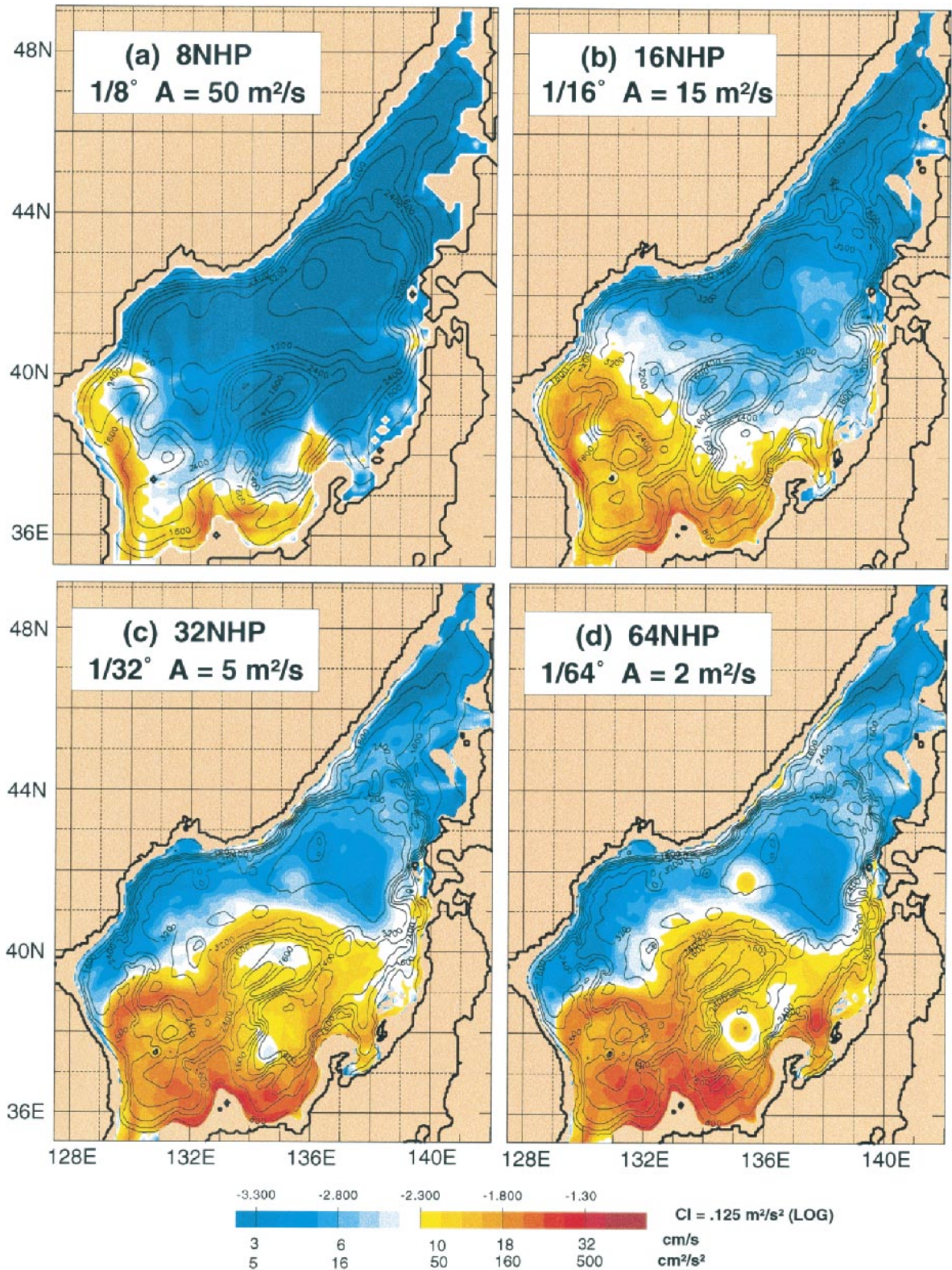


FIG. 12. Surface layer EKE per unit mass (color) and bottom topography (black contours) for the same simulations shown in Fig. 9: (a)  $\frac{1}{8}^\circ$  resolution (8NHP), (b)  $\frac{1}{16}^\circ$  resolution (16NHP), (c)  $\frac{1}{32}^\circ$  resolution (32NHP), and (d)  $\frac{1}{64}^\circ$  resolution (64NHP). Contour interval of EKE is  $0.125 \log_{10} \text{m}^2 \text{s}^{-2}$ , and is also expressed in  $\text{cm s}^{-1}$  (mean speed) and  $\text{cm}^2 \text{s}^{-2}$  (EKE per unit mass). Contour interval of bottom topography is 400 m.

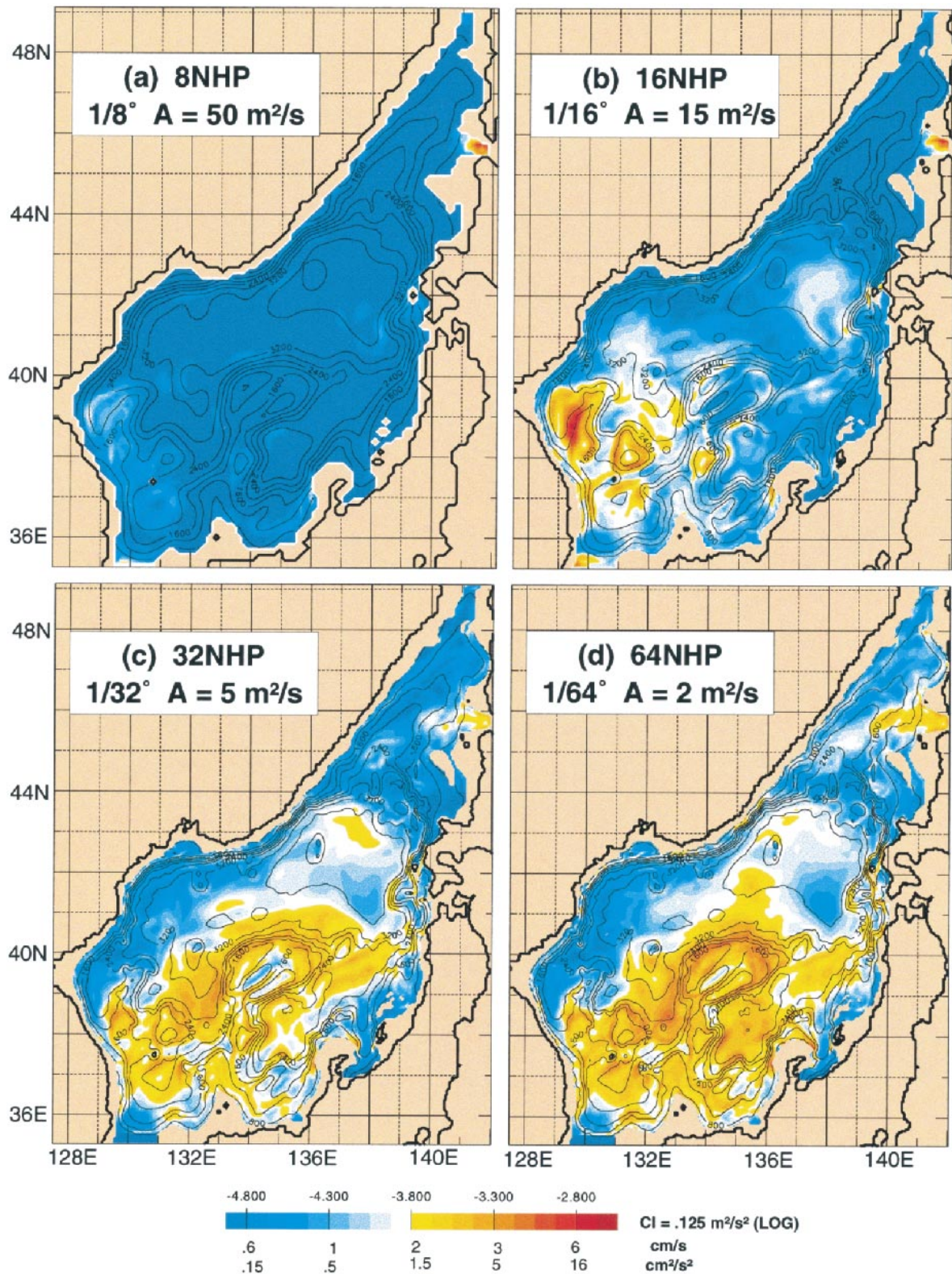


FIG. 13. Abyssal layer EKE per unit mass (color) and bottom topography (black contours) for the same simulations shown in Fig. 9: (a)  $1/8^\circ$  resolution (8NHP), (b)  $1/16^\circ$  resolution (16NHP), (c)  $1/32^\circ$  resolution (32NHP), and (d)  $1/64^\circ$  resolution (64NHP). Contour interval of EKE is  $0.125 \log_{10} \text{m}^2 \text{s}^{-2}$ , and is also expressed in  $\text{s}^{-1}$  (mean speed) and  $\text{cm}^2 \text{s}^{-2}$  (EKE per unit mass). Contour interval of bottom topography is 400 m.

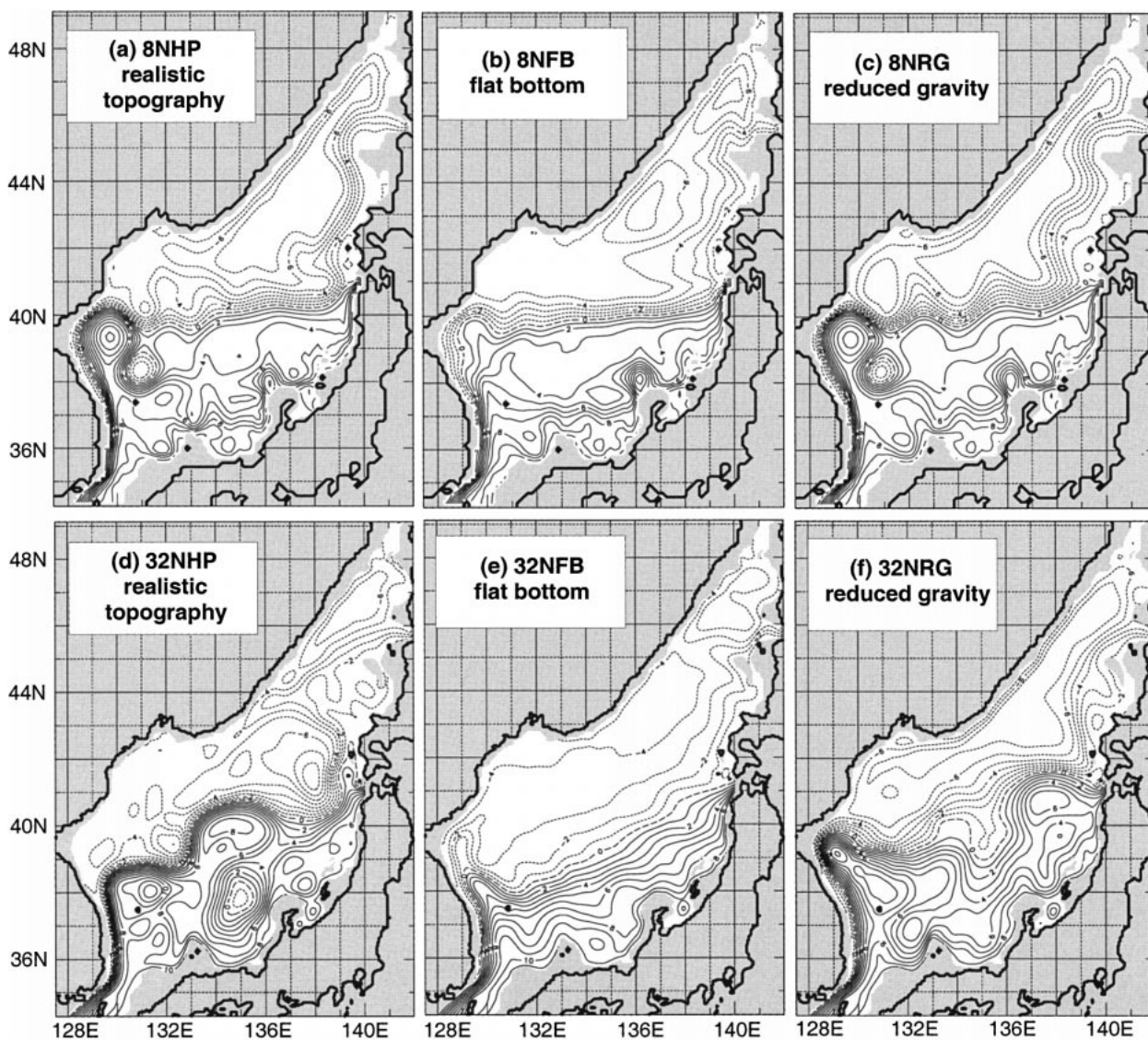


FIG. 14. Mean SSH from  $1/6^\circ$  nonlinear simulations with (a) realistic bottom topography (8NHP), (b) a flat bottom (8NFB), and (c) a reduced gravity version (8NRG). Panels (d)–(f) are the same except for  $1/32^\circ$  resolution. Realistic separation of the EKWC is only achieved in simulation 32NHP. Contour interval is 1 cm.

ulation 8NFB (Fig. 14b) shows notable deviations from simulations 8NRG and 8NHP and therefore a substantial impact of the barotropic mode. The relatively high abyssal EKE in the southern half of the basin in simulation 8NFB (not shown) indicates that baroclinic instability is mainly responsible. Baroclinic instability is an efficient process for surface to abyssal KE transfer and it is the only mechanism that can explain the larger EKE and stronger abyssal currents in 8NFB, because it is the only possibility that was either absent or inhibited in the other two simulations.

In baroclinic instability involving the barotropic mode, the abyssal circulation plays an essential role. Rapid vortex stretching and compression associated with rapidly moving upper ocean eddies (compared to

nondispersive Rossby wave propagation) efficiently transfers energy to the abyssal layer, generating closed abyssal circulation eddies with a quarter wavelength offset from the surface layer. When strongly sloping bottom topography is present, the  $f/h$  contours of the topography tend to inhibit baroclinic instability by inhibiting the formation of the associated abyssal circulation eddies [because the conservation of potential vorticity limits the crossing of  $f/h$  contours depending on the relative amplitudes of the relative and planetary vorticity; e.g., see section 5.5 of Hurlburt (1986)]. In addition, Hurlburt et al. (1990) contains a clear illustration of a baroclinically unstable event and a comparison to one that is barotropically unstable (see their section 3 and Figs. 4 and 5). Thus, the upper ocean circulation of simulation

8NHP with realistic bottom topography is more like that of reduced gravity simulation 8NRG than flat bottom simulation 8NFB.

The mean SSH fields for simulations 32NHP, 32NFB, and 32NRG are examined (Figs. 14d–f, respectively). At  $\frac{1}{32}^\circ$  resolution all three simulations show striking differences from each other as well as changes from their  $\frac{1}{8}^\circ$  counterparts. For example, simulation 32NHP shows separation of the EKWC from the Korean coast near  $37^\circ\text{N}$ , unlike its  $\frac{1}{8}^\circ$  counterpart (8NHP) which shows EKWC separation at  $40^\circ$ – $41^\circ\text{N}$ , as do both of the reduced-gravity simulations (8NRG and 32NRG). Simulation 32NFB also shows EKWC overshoot of the observed separation latitude and at least weak northward western boundary current flow as far north as  $42^\circ\text{N}$ , while 32NHP shows southward flow along this coast as far as  $37^\circ\text{N}$ . A similar situation is found in the abyssal layer (not shown). The upper ocean circulation of simulation 32NHP exhibits many other departures from simulations 32NFB and 32NRG, which are clearly related to the bottom topography as discussed next.

The upper ocean–topographical coupling that allows the EKWC to separate near the observed latitude requires stronger baroclinic instability and larger amplitude abyssal layer relative vorticity (generated by vortex compression and stretching) than occurred at  $\frac{1}{8}^\circ$  or  $\frac{1}{16}^\circ$  resolution. This is possible only when mesoscale flow instabilities are very well resolved. At least  $\frac{1}{32}^\circ$  resolution was needed in the JES simulations. This resolution is substantially finer than the first internal Rossby radius of deformation, which is resolved even in the  $\frac{1}{8}^\circ$  simulations. The coupling mechanism relies on the fact that baroclinic instability is very efficient at transferring energy down to the abyssal layer and that energized deep flows tend to follow the  $f/h$  contours in the abyssal layer as required by the conservation of potential vorticity. Using the continuity equation, Hurlburt and Thompson (1980) show how abyssal currents can steer upper ocean currents in a two-layer model since

$$\mathbf{v}_{1g} \cdot \nabla h_1 = \mathbf{v}_{2g} \cdot \nabla h_1, \quad (4)$$

where  $\mathbf{v}_{kg}$  is the geostrophic velocity in layer  $k$  and the left-hand side of (4) is the geostrophic advective contribution to the mass divergence term in the continuity equation (3) for layer 1. The geostrophic balance for the internal mode is given by

$$\mathbf{k} \times f(\mathbf{v}_{1g} - \mathbf{v}_{2g}) = g' \nabla h_1, \quad (5)$$

where  $g' = (\rho_2 - \rho_1)/\rho_0$ . In essence, if  $\mathbf{v}_{1g} \gg \mathbf{v}_{2g}$ , then (4) and (5) state that if  $\nabla h_1$  is a good measure of  $\mathbf{v}_{1g}$ , then in a two-layer model the currents in the lower layer can advect gradients of upper-layer thickness and thus steer upper-layer currents, especially where the currents intersect at large angles. This argument formally breaks down in multilayer models, but the steering effect remains in situations where the barotropic and first baroclinic modes are dominant (Hurlburt et al. 1996; Hurl-

burt and Metzger 1998), a situation which exists in the JES.

The cycle of upper ocean–topographical coupling is summarized in Fig. 15. Baroclinically unstable surface currents efficiently transfer energy to the abyssal layer. The resulting abyssal flow follows the  $f/h$  contours of the bottom topography to conserve potential vorticity (Fig. 15b). The mean surface layer currents are strongly influenced by the bottom topography even though they do not impinge on the bottom topography (Fig. 15a). The EKWC separates from the coast of Korea where the southward abyssal flow near the coast is interrupted by anticyclonic flow around the ridge near  $129.5^\circ\text{E}$ ,  $38.4^\circ\text{N}$  in the bottom topography. Offshore, near  $130^\circ\text{E}$  the latitude of the eastward flow associated with this deep anticyclonic eddy coincides with the southern boundary of another strong southward abyssal current. While the topographic steering is strongest where upper ocean and abyssal currents intersect at large angles, the end result is upper ocean and abyssal currents that are nearly parallel in many locations as seen in Fig. 15.

Figure 16 demonstrates unequivocally that the bottom topography in this region is critical for separation of the EKWC to occur near the observed latitude of  $37^\circ$ – $38^\circ\text{N}$ . Figures 16a,b are simply enlargements of Figs. 15a,b in the region of the EKWC. Figures 16c,d are the same except from simulation 32NHPb, which is identical to simulation 32NHP except that all of the bottom topography shallower than 2000 m (excluding the continental slope) in the region where the EKWC separates from the coast, particularly the north–south oriented ridge, has been set to a constant depth of 2000 m. This modification removes the topographic features required to constrain the deep mean flows in this region (Fig. 16d), thereby removing their influence on the surface circulation. As a result, in simulation 32NHPb the EKWC overshoots too far to the north, similar to simulation 8NHP (although simulation 32NHPb is clearly more realistic than 8NHP where the bottom topography was not modified).

The similarity of  $\frac{1}{8}^\circ$  simulations 8NHP (realistic topography) and 8NRG (reduced gravity) suggests that realistic bottom topography plays no role in realistic separation of the EKWC nor in the surface layer JES circulation in general. However, that is an incorrect conclusion. Only when the results from the  $\frac{1}{32}^\circ$  simulations are examined does the importance of the bottom topography become clear since only the  $\frac{1}{32}^\circ$  simulation (32NHP) with realistic bottom topography shows an EKWC that separates at a realistic latitude (when HR wind plus straits forcing is used). This result is significant because, if the  $\frac{1}{32}^\circ$  simulations had not been performed, an incorrect conclusion concerning the role of the bottom topography would have been reached. Unfortunately, this scenario may be more common than not, as few ocean models are economical enough at present to run with such high resolution on a basin-scale domain.

# Upper Ocean - Topographic Coupling

## 1/32° 4-layer Japan/East Sea Model

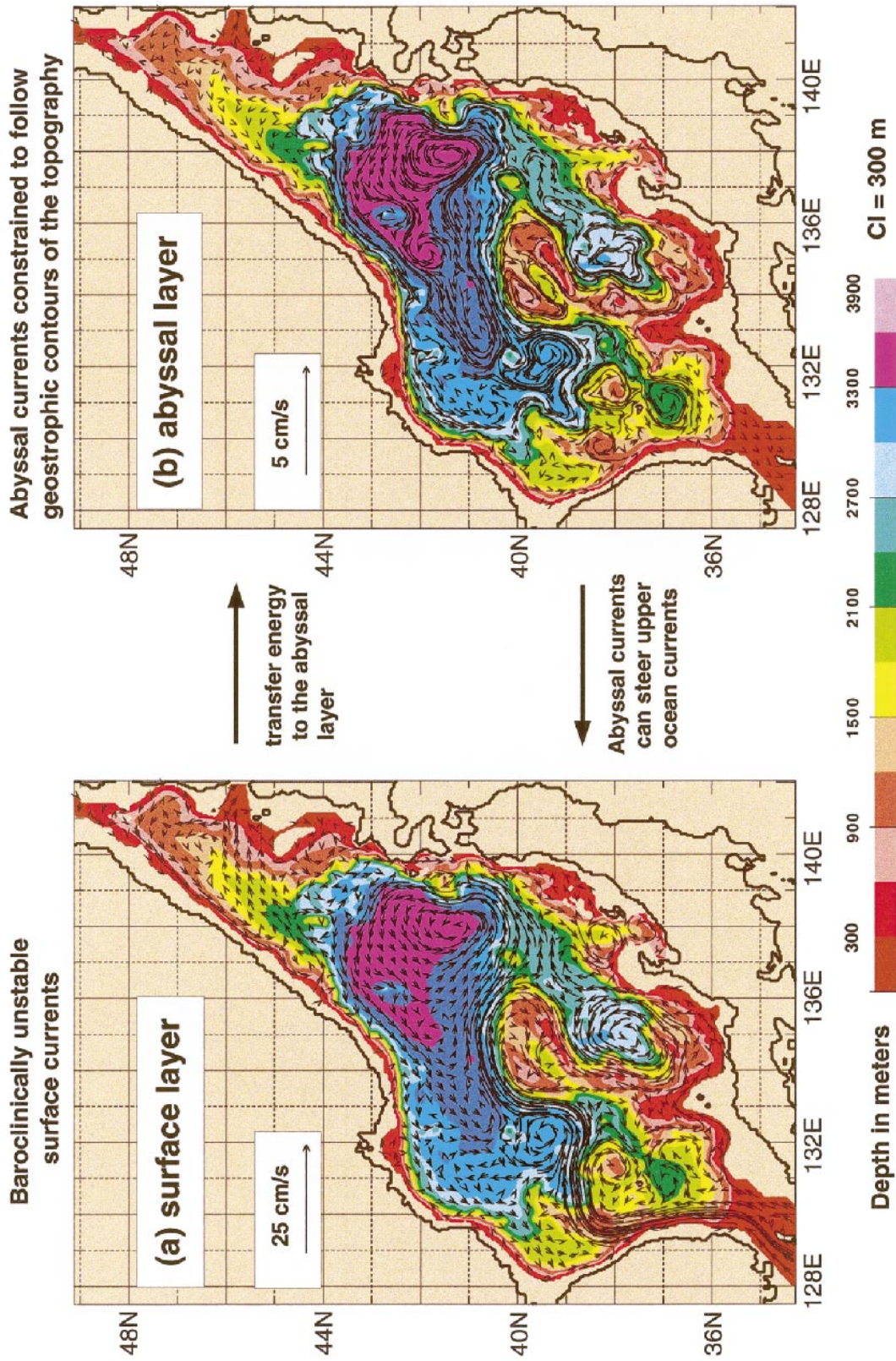


FIG. 15. Bottom topography and mean currents for (a) the surface layer, and (b) the abyssal layer. This figure illustrates the dynamics of upper ocean-topographical coupling via mesoscale flow instabilities (mixed baroclinic-barotropic).

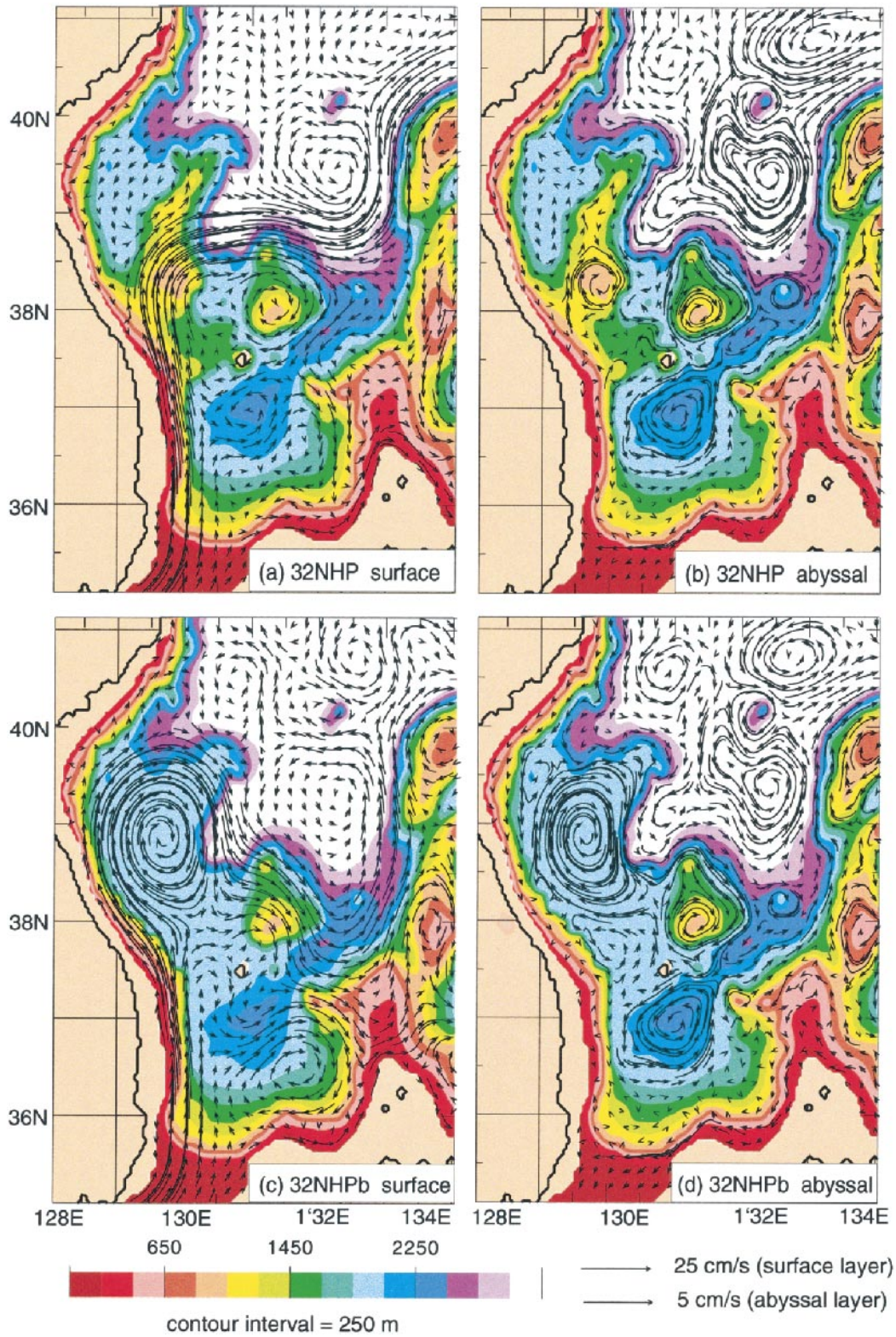


FIG. 16. Bottom topography (color) and mean currents from simulation 32NHP in the region where the EKWC separates from the coast of Korea for (a) the surface layer, and (b) the abyssal layer. The same is shown in (c) and (d) for simulation 32NHPb, which has the topographic high located near 39°N, 130°E removed.



## 7. Summary and conclusions

An ensemble of layered ocean simulations with increasing dynamical complexity has been used to investigate the circulation dynamics in the JES. The simulations used horizontal resolution that ranged from  $\frac{1}{8}^\circ$  to  $\frac{1}{64}^\circ$  for each variable and vertical resolution that ranged from 1.5-layer reduced-gravity to four-layer finite depth with realistic bottom topography. All include a free surface and realistic coastline geometry. Most were forced by prescribed seasonally varying transports through the Tsushima, Tsugaru, and Soya Straits and by the Hellerman and Rosenstein (1983; HR) monthly wind stress climatology, but two were forced with a monthly climatology formed from the 1979–1993 ECMWF 10-m reanalysis winds. The modularity of the NLOM allowed certain dynamical processes to be included, excluded, or varied, revealing the impact of specific dynamical processes on circulation features in the JES.

Linear versions of the model revealed the impact of the wind and throughflow forcing, separately and collectively. The linear versions of the model depicted the TWC as a Munk (1950) western boundary layer with a Sverdrup (1947) interior. In these simulations, the large-scale circulation was dominated by the throughflow forcing, but the LCC was only reproduced when wind forcing was included. Most of the basic current systems can be reproduced with a linear version of the model forced with (both) throughflow forcing and the HR wind stress climatology. A major exception is the absence of the NB, which is observed to flow northeastward along the Honshu coast. Instead, the linear simulations show unrealistic southwestward flow along the Honshu coast with HR wind stress forcing present and no flow along this coast with the throughflow forcing (only). The NKCC is also missing because the separation latitude of the EKWC is too far north.

Nonlinear versions of the model include higher order dynamical processes, such as flow instabilities, inertial jets and boundary layers, and isopycnal outcropping via interface ventilation when some combination of realistic bottom topography, the barotropic mode, and multiple internal modes are included. Nonlinear simulations were much more realistic than their linear counterparts and have inertial currents and fronts that form meanders and rings at all resolutions used in this study. The  $O(1)$  variations in layer thickness allow for the possibility of isopycnal outcropping via ventilation of model interfaces. For the NLOM, isopycnal outcropping is crucial for the formation of the NB and has substantial impact on other aspects of the JES circulation, including the LCC and water mass formation. In a  $\frac{1}{8}^\circ$  simulation forced with seasonal throughflow and the HR monthly wind stress climatology, the residence time for Japan/East Sea Proper Water, the abyssal layer in the model, is about 130 years. This is consistent with observationally based estimates of about 80 years by Kim and Kim (1997). Some authors (e.g., Yoon 1982; Kawabe, 1982)

have suggested topographic control as a mechanism for the NB, but the nonlinear simulations performed here suggest isopycnal outcropping as an alternate explanation.

All major current systems in the JES are realistically simulated at  $\frac{1}{8}^\circ$  except that the EKWC separates from the Korean coast farther to the north than the observed latitude when the model is forced with the HR monthly wind stress climatology. More realistic separation of the EKWC can be achieved when the model is forced with a different wind climatology, such as the climatology formed from the 1979–1993 ECMWF 10-m reanalysis winds used in this study. The more realistic separation latitude of the EKWC is due to the stronger positive wind stress curl north of the separation latitude in this wind product. This result suggests that great care must be exercised in the interpretation of model results, since the external forcing might provide a realistic depiction of the current systems without including all the relevant dynamics. Since the HR climatology resulted in overshoot of the EKWC at  $\frac{1}{8}^\circ$  resolution, increased realism at higher resolution is due to changes in the dynamics, not the external forcing.

When forced with HR winds, overshoot of the EKWC persists at  $\frac{1}{16}^\circ$  resolution. However, when  $\frac{1}{32}^\circ$  resolution is used, the EKWC separates from the coast near the observed latitude between  $37^\circ$  and  $38^\circ\text{N}$ . This change in the behavior of the EKWC as a function of grid resolution is accompanied by much higher levels of upper ocean and abyssal EKE at higher resolution and distinct changes in the abyssal circulation. Specifically, the  $\frac{1}{8}^\circ$  simulation shows a weak anticyclonic abyssal circulation, whereas the  $\frac{1}{32}^\circ$  simulation shows stronger, cyclonic deep flows. Maps of EKE in the surface and abyssal layers show geographical collocation of high EKE in these layers, indicating the presence of baroclinic instability. This instability (actually mixed baroclinic–barotropic) is very efficient at transferring energy downward. Once the energy is transferred into the lowest layer, it energizes the abyssal flow, which is constrained to follow the  $f/h$  contours of the bottom topography. The abyssal circulation can then influence the surface circulation via a process described in Hurlburt and Thompson (1980) and Hurlburt et al. (1996), even when the upper-ocean flow does not impinge on the bottom topography. This cycle of upper ocean–topographical coupling requires sufficient levels of baroclinic instability, which were only attained at  $\frac{1}{32}^\circ$  resolution and higher. Hence, this effect is missed at coarser resolution.

The roles of high horizontal grid resolution and realistic bottom topography are strongly interrelated. The  $\frac{1}{8}^\circ$  simulations that have a bottom layer that is infinitely deep and at rest (i.e., reduced-gravity) and include HR and throughflow forcing are very similar to those with realistic bottom topography, including almost identical overshoot of the EKWC. Corresponding  $\frac{1}{8}^\circ$  flat-bottom simulations show significant differences from these, but

again show the EKWC overshoot. This result suggests that realistic bottom topography is unimportant for realistic separation of the EKWC. However, when a corresponding trio of three model simulations is performed at  $\frac{1}{32}^\circ$  resolution, only the case with realistic bottom topography depicts realistic separation of the EKWC. Moreover, realistic separation is dependent on a specific, relatively shallow topographic feature near the Korean coast. When this topographic feature is removed, the EKWC separates too far to the north. Hence, simply using high horizontal resolution to generate mesoscale flow instabilities is not sufficient, in and of itself, for attaining upper ocean–topographical coupling; realistic bottom topography is also required, particularly to attain separation of the EKWC at the observed latitude.

The mean pathways of the current systems from the  $\frac{1}{32}^\circ$  and  $\frac{1}{64}^\circ$  simulations are quite similar, as are the surface and abyssal EKE from these simulations, with some notable exceptions in the southern JES. In contrast, when the resolution was increased from  $\frac{1}{8}^\circ$  to  $\frac{1}{16}^\circ$  or from  $\frac{1}{16}^\circ$  to  $\frac{1}{32}^\circ$ , the changes in the solutions were quite dramatic. This comparison suggests that statistical equilibrium for mesoscale variability has been nearly achieved at  $\frac{1}{32}^\circ$  resolution. This convergence is significant since a doubling of the horizontal grid resolution usually results in significant changes in the model solution. In short, the results presented in this paper describe the process by which the surface circulation can be influenced by the abyssal circulation through mesoscale flow instabilities. The mechanism by which this occurs, known as upper ocean–topographical coupling, requires that mesoscale eddies be very well resolved as well as the presence of realistic bottom topography. Well-resolved eddies, certainly those smaller than the internal Rossby deformation radius, are needed to generate sufficient flow instabilities and the presence of the bottom topography serves to steer upper ocean currents and to regulate the strength and location of the flow instabilities. In numerical ocean models, the coupling requires high horizontal grid resolution, at least  $\frac{1}{32}^\circ$  in the JES. Thus, the role of upper ocean–topographical coupling is missed in coarser resolution models, which can lead to unexplained errors in the mean pathways of the current systems.

*Acknowledgments.* This is a contribution to the Japan/East Sea Departmental Research Initiative (DRI) sponsored by the Office of Naval Research (ONR) under Program Element 601153N. The 6.1 Low Latitude Western Boundary Currents (LLWBC) project under the same program element provided matching funds in FY98. The 6.2 Global Ocean Prediction System project contributed in earlier years under Program Element 602435N. The simulations were performed on Sun workstations, the Cray T3E and YMP at the Naval Oceanographic Office, the Cray T3E at the Army High Performance Computer Resource Center, and the Cray T3D and T3E at the Arctic Region Supercomputing

Center. The nonworkstation computations were performed under grants of computer time from the Defense Department High Performance Computing Initiative. Dr. Alan Wallcraft is recognized for substantial contribution to this effort through his work on model development and his computer expertise.

#### REFERENCES

- An, H., K. Kim, and H. R. Shin, 1994: On the warm eddies in the southwestern part of the East Sea (the Japan Sea). *J. Korean Soc. Oceanogr.*, **29**, 152–163.
- Beardsley, R. C., R. Limeburner, K. Kim, and J. Candela, 1992: Lagrangian flow observations in the East China, Yellow, and Japan Seas. *La Mer*, **30**, 297–314.
- Bleck, R., C. Rooth, D. Hu, and L. Smith, 1992: Salinity-driven thermocline transients in a wind- and thermohaline-forced isopycnal coordinate model of the North Atlantic. *J. Phys. Oceanogr.*, **22**, 1486–1505.
- Cho, Y. K., and K. Kim, 1996: Seasonal variation of the East Korea Warm Current and its relation with the cold water. *La Mer*, **34**, 172–182.
- Gibson, J. K., P. Kallberg, S. Uppala, A. Hernandez, A. Nomura, and E. Serrano, 1997: ERA description. ECMWF Re-Analysis Project Report Series 1, ECMWF, Reading, Berkshire, United Kingdom, 71 pp.
- Hellerman, S., and M. Rosenstein, 1983: Normal monthly wind stress over the world ocean with error estimates. *J. Phys. Oceanogr.*, **13**, 1093–1104.
- Holland, W. R., and L. B. Lin, 1975: On the generation of mesoscale eddies and their contribution to the oceanic general circulation. I. A preliminary numerical experiment. *J. Phys. Oceanogr.*, **5**, 642–657.
- Holloway, G., 1992: Representing topographic stress for large-scale ocean models. *J. Phys. Oceanogr.*, **22**, 1033–1046.
- , T. Sou, and M. Eby, 1995: Dynamics of circulation of the Japan Sea. *J. Mar. Res.*, **53**, 539–569.
- Hurlburt, H. E., 1986: Dynamic transfer of simulated altimeter data into subsurface information by a numerical ocean model. *J. Geophys. Res.*, **91**, 2372–2400.
- , and J. D. Thompson, 1980: A numerical study of Loop Current intrusions and eddy shedding. *J. Phys. Oceanogr.*, **10**, 1611–1651.
- , and E. J. Metzger, 1998: Bifurcation of the Kuroshio Extension at the Shatsky Rise. *J. Geophys. Res.*, **103**, 7549–7566.
- , D. N. Fox, and E. J. Metzger, 1990: Statistical inference of weakly correlated subthermocline fields from satellite altimeter data. *J. Geophys. Res.*, **95**, 11 375–11 409.
- , A. J. Wallcraft, W. J. Schmitz Jr., P. J. Hogan, and E. J. Metzger, 1996: Dynamics of the Kuroshio/Oyashio current system using eddy-resolving models of the North Pacific Ocean. *J. Geophys. Res.*, **101**, 941–976.
- Ichiye, T., 1984: Some problems of circulation and hydrography of the Japan Sea and the Tsushima Current. *Ocean Hydrodynamics of the Japan and East China Seas*, T. Ichiye, Ed., Elsevier, 15–54.
- Kawabe, M., 1982: Branching of the Tsushima Current in the Japan Sea. II. Numerical experiment. *J. Oceanogr. Soc. Japan*, **38**, 183–192.
- Kim, C. H., and J. Y. Yoon, 1994: A numerical study on the seasonal variation of the Tsushima Warm Current along the coast of Japan. *Proc. Third CREAMS Workshop*, Seoul, Korea, Research Institute of Oceanography, Seoul National University, 73–79.
- Kim, K., and J. Y. Chung, 1984: On the salinity minimum and dissolved oxygen maximum layer in the East Sea (Sea of Japan). *Ocean Hydrodynamics of the Japan and East China Seas*, T. Ichiye, Ed., Elsevier, 55–65.
- , and R. Legeckis, 1986: Branching of the Tsushima Current in

- 1981–83. *Progress in Oceanography*, Vol. 17, Pergamon, 265–276.
- , and J. Y. Yoon, 1996: Modeling of the wind-driven circulation in the Japan Sea using a reduced gravity model. *J. Oceanogr.*, **52**, 359–373.
- , and K. Kim, 1997: What is happening in the East Sea (Japan Sea)? Recent chemical observations during CREAMS 93–96. *J. Korean Soc. Oceanogr.*, **31**, 164–172.
- Kwizak, M., and A. J. Robert, 1971: A semi-implicit scheme for grid point atmospheric models of the primitive equations. *Mon. Wea. Rev.*, **99**, 32–36.
- Levitus, S., 1982: *Climatological Atlas of the World Ocean*. NOAA Prof. Paper No. 13, U.S. Govt. Printing Office, 173 pp.
- Lie, H.-J., M.-S. Suk, and C. Kim, 1989: Observations of south-eastward deep currents off the west coast of Korea. *J. Oceanol. Soc. Korea*, **24**, 63–68.
- , S. K. Byun, I. Band, and C. H. Cho, 1995: Physical structure of eddies in the southwestern East Sea. *J. Korean Soc. Oceanogr.*, **30**, 170–183.
- Luyten, J. R., J. Pedlosky, and H. Stommel, 1983: The ventilated thermocline. *J. Phys. Oceanogr.*, **13**, 292–309.
- Mesinger, F., and A. Arakawa, 1976: Numerical methods used in atmospheric models. GARP Publ. Ser., No. 17, WMO, 64 pp.
- Miyazaki, M., 1952: The heat budget in the Japan Sea (in Japanese). *Bull. Hokkaido Reg. Fish. Res. Lab.*, **4**, 1–54.
- Moore, D. R., and A. J. Wallcraft, 1998: Formulation of the NRL Layered Ocean Model in spherical coordinates. Naval Research Laboratory Rep. NRL CR 7323-96-0005, Naval Research Laboratory, Stennis Space Center, 24 pp. [Available from Naval Research Laboratory, Stennis Space Center, MS 39529.]
- Moriyasu, S., 1972: The Tsushima Current. *Kuroshio: Its Physical Aspects*, H. Stommel and K. Yoshida, Eds., University of Tokyo Press, 353–369.
- Munk, W. H., 1950: On the wind-driven ocean circulation. *J. Meteor.*, **7**, 79–93.
- Na, J.-Y., J. W. Seo, and S. K. Han, 1992: Monthly mean sea surface winds over the adjacent seas of the Korean Peninsula (in Korean). *J. Oceanol. Soc. Korea*, **27**, 1–10.
- Naganuma, K., 1977: The oceanographic fluctuations in the Japan Sea. *Kaiyo Kayaku*, **9**, 137–141.
- National Oceanic and Atmospheric Administration, 1988: Digital relief of the surface of the earth. Data Ann. 88-MGG-02. [Available online at <http://www.ngdc.noaa.gov:80/mgg/global/setopo.html>.]
- Orlanski, I., 1976: A simple boundary condition for unbounded hyperbolic flows. *J. Comput. Phys.*, **21**, 251–269.
- Preller, R. H., and P. J. Hogan, 1998: Oceanography of the Sea of Okhotsk and the Japan/East Sea. *The Sea*, Vol. 11: *The Global Coastal Ocean, Regional Studies and Synthesis*, A. R. Robinson and K. H. Brink, Eds., John Wiley and Sons, 429–481.
- Senjyu, T., and H. Sudo, 1994: The upper portion of the Japan Sea Proper Water: Its source and circulation as deduced from isopycnal analysis. *J. Oceanogr.*, **50**, 663–690.
- Seung, Y.-H., 1997: Application of ventilation theory to the East Sea. *J. Korean Soc. Oceanogr.*, **32**, 8–16.
- , and K.-J. Kim, 1993: A numerical modeling of the East Sea circulation. *J. Oceanol. Soc. Korea*, **28**, 292–304.
- , and —, 1995: A multilayer model for dynamics of upper and intermediate layer circulation of the East Sea. *J. Korean Soc. Oceanogr.*, **30**, 227–236.
- , and J.-H. Yoon, 1995a: Some features of winter convection in the Japan Sea. *J. Oceanogr.*, **51**, 61–73.
- , and —, 1995b: Robust diagnostic modeling of the Japan Sea circulation. *J. Oceanogr.*, **51**, 421–440.
- , and K.-J. Kim, 1997: Estimation of the residence time for renewal of the East Sea Intermediate Water using MICOM. *J. Korean Soc. Oceanogr.*, **32**, 17–27.
- Shriver, J. F., and H. E. Hurlburt, 1997: The contribution of the global thermohaline circulation to the Pacific to Indian Ocean through-flow via Indonesia. *J. Geophys. Res.*, **102**, 5491–5511.
- Suda, K., and K. Hidaka, 1932: The results of the oceanographical observations on board R.M.S. *Syunpu Maru* in the southern part of the Sea of Japan in the summer of 1929, part 1 (in Japanese). *J. Oceanogr. Imp. Mar. Obs.*, **3**, 291–375.
- Sverdrup, H. U., 1947: Wind-driven currents in a baroclinic ocean: With application to the equatorial currents of the eastern Pacific. *Proc. Natl. Acad. Sci. U.S.A.*, **33**, 318–326.
- Toba, Y., K. Tomizawa, Y. Kurasawa, and K. Hanawa, 1982: Seasonal and year to year variability of the Tsushima–Tsugaru Warm Current system with its possible cause. *La Mer*, **20**, 41–51.
- Uda, M., 1934: The results of simultaneous oceanographical investigations in the Japan Sea and its adjacent waters in May and June, 1932 (in Japanese) *J. Imp. Fish. Exp. Stn.*, **5**, 57–190.
- Vasilev, A. S., and V. P. Makashin, 1992: Ventilation of the Japan Sea waters in winter. *La Mer*, **30**, 169–177.
- Wallcraft, A. J., 1991: The Navy Layered Ocean Model users guide. NOARL Rep. 35, Naval Research Laboratory, Stennis Space Center, MS, 21 pp. [Available from Naval Research Laboratory, Stennis Space Center, MS 39529.]
- , and D. R. Moore, 1997: A scalable implementation of the NRL Layered Ocean Model. *Parallel Comput.*, **23**, 2227–2242.
- Yarichin, V. G., 1980: Steady state of the Japan Sea circulation (in Russian). *Problems of Oceanography*, V. V. Pokudov, Ed., Hydrometeoizdat, Leningrad, 46–61.
- Yi, S. U., 1966: Seasonal and secular variations of the water volume transport across the Korea Strait. *J. Oceanol. Soc. Korea*, **1**, 7–13.
- Yoon, J. H., 1982: Numerical experiment on the circulation in the Japan Sea. Part III, Mechanism of the Nearshore Branch of the Tsushima Current. *J. Oceanogr. Soc. Japan.*, **38**, 125–130.